Computational Geosciences (2020) 24:641–661
https://doi.org/10.1007/s10596-019-09851-6

ORIGINAL PAPER

Fast flow computation methods on unstructured tetrahedral meshes for rapid reservoir modelling

Zhao Zhang[1,2] · Sebastian Geiger[1] · Margaret Rood[3] · Carl Jacquemyn[3] · Matthew Jackson[3] · Gary Hampson[3] · Felipe Moura De Carvalho[4] · Clarissa Coda Marques Machado Silva[4] · Julio Daniel Machado Silva[4] · Mario Costa Sousa[4]

Received: 29 October 2018 / Accepted: 20 June 2019 /Published online: 28 June 2019

Abstract

Subsurface reservoir models have a high degree of uncertainty regarding reservoir geometry and structure. A range of conceptual models should therefore be generated to explore how fluids-in-place, reservoir dynamics, and development decisions are affected by such uncertainty. The rapid reservoir modelling (RRM) workflow has been developed to prototype reservoir models across scales and test their dynamic behaviour. RRM complements existing workflows in that conceptual models can be prototyped, explored, compared, and ranked rapidly prior to detailed reservoir modelling. Reservoir geology is sketched in 2D with geological operators and translated in real-time into geologically correct 3D models. Flow diagnostics provide quantitative information for these reservoir model prototypes about their static and dynamic behaviours. A tracing algorithm is reviewed and implemented to compute time-of-flight and tracer concentrations efficiently on unstructured grids. Numerical well testing (NWT) is adopted in RRM to further interrogate the reservoir model. A new edge-based fast marching method is developed and implemented to solve the diffusive time-of-flight for approximating pressure transients efficiently on unstructured tetrahedral meshes. We demonstrate that an implementation of the workflow consisting of integrated sketch-based interface modelling, unstructured mesh generation, flow diagnostics, and numerical well testing is possible.

Keywords Unstructured tetrahedral mesh · Flow diagnostics · Numerical well testing · Rapid reservoir modelling

1 Introduction

The spatial distribution of multiscale geological heterogeneities in subsurface reservoirs, for example hydrocarbon and geothermal reservoirs or saline aquifers for CO_2 storage, is uncertain in the subsurface. To assess the impact of this uncertainty, a number of reservoir models are typically built, ranked, and compared for reservoir appraisal. Additionally, we may also want to know how changing well placements and controls affect fluid flow in the reservoir while also considering uncertainties in the geological structures and distribution of petrophysical properties. Conventional workflows consisting of detailed geological modelling and full-physics transient simulation could be used for such ranking and exploring purposes but this approach can be time-consuming. The slow turnaround time of conventional workflows is one of the reasons that geological concepts are commonly locked-in early during reservoir development, i.e. the time when economic uncertainty is greatest, without exploring different conceptual models [6, 10]. However, different conceptual models may yield considerably different and distinct predictions of reservoir volumes, fluid flow patterns, and optimal development strategies during the life time of a field [2, 7, 49]. Therefore, it is desirable to develop a tool to rapidly prototype models and rank various concepts prior to detailed full-physics reservoir modelling and simulation.

Realising the importance and challenge of exploring conceptual models efficiently [31] has introduced the rapid reservoir modelling (RRM) workflow and software com-

✉ Zhao Zhang
zzhang6666@163.com

1 Institute of Petroleum Engineering, Heriot-Watt University, Edinburgh, EH14 4AS, UK

2 Present address: Petroleum Engineering School, Southwest Petroleum University, Chengdu, 610500, China

3 Department of Earth Science and Engineering, Imperial College London, London, SW7 2AZ, UK

4 Department of Computer Science, University of Calgary, Calgary, T2N 1N4, Canada

bining techniques of sketch-based interface and modelling (SBIM) [47], automatic geological operators, unstructured tetrahedral meshes, flow diagnostics, and numerical well testing. The aim of RRM is not to replace full-physics simulation, which with recent development in computer science is becoming less time-consuming, but to provide a tool for prototyping, building, and ranking conceptual models efficiently without consuming much computational resources, especially in scenarios where little data is available and geological uncertainty is large. SBIM allows users to build surface-based reservoir models (SBRM) [9, 24, 25, 29–34, 38, 39, 48, 53, 71] by sketching geology directly on computer screens, in a manner that is intuitive, interactive, and efficient. The advantage of SBRM is that geological heterogeneities across multiple scales can be accurately modelled by surfaces. The drawback is that heterogeneity can only described by introducing surface boundaries. This excludes a systematic application of the conventional property modelling techniques and makes the models very complex if realistic sedimentary features must be represented at reservoir scale. While the performance gain of RRM will be lost if such a resolution is attempted, RRM can be used to quickly upscale small-scale geological features to estimate effective properties that can be used at larger scales.

3D models can be created from 2D surfaces by sketching on multiple cross-sections or by extrapolation in 3D. In the process of sketching, geological operators are automatically implemented to ensure the model is geologically correct [51]. In SBRM, geological heterogeneities are represented by discrete volumes bounded by surfaces. Therefore, the model is grid-independent. Grids are built on-the-fly and only when needed for hydrocarbon-in-place estimation, flow diagnostics, and numerical well testing. Unstructured tetrahedral meshes are generated adapting to the bounding surfaces such that complex reservoir geometries can be preserved [43]. There are many algorithm and software tools to generate unstructured tetrahedral meshes. In RRM, we incorporate the Delaunay-based mesh generator TetGen [61].

Flow diagnostics refer to numerical experiments to probe a reservoir model efficiently [58]. The basis of flow diagnostics is the distribution of time-of-flight (TOF) and tracer concentrations (TC). TOF is the time it takes for a fluid particle to travel from an inflow boundary to its current location. TC denotes the percentage of flow coming from an inflow boundary associated with the tracer. TOF and TC provide qualitative 3D visualisation of unswept regions and dynamic well connectivity, as well as swept and drained reservoir areas. While flow diagnostics can be obtained based on streamline methods for nearly orthogonal structured grids [5, 64], it is challenging to trace streamlines accurately for general corner-point and unstructured meshes [27, 41, 50]. Therefore, [58] solved TOF and TC directly on the grid blocks of the reservoir model by use of the finite volume method for flow diagnostics. The cells are reordered by a depth-first-search algorithm such that TOF and TC can be computed locally volume-by-volume [46]. Flow diagnostics were later applied to reservoir development optimisation [45]. Additional properties such as the dynamic Lorenz coefficient [60] can be easily computed from the TOF distribution and provide further insight in the dynamic behaviour of a reservoir.

The prerequisite of solving TOF and TC is a velocity field which can be exported from a detailed multiphase flow simulation or computed directly given a steady-state assumption [37]. The two-point flux approximation is consistent for K-orthogonal grids, but unstructured tetrahedral meshes are usually not K-orthogonal. Therefore, the control volume finite element method (CVFEM), which essentially uses a multi-point flux approximation (MPFA) and is consistent on unstructured tetrahedral meshes [22, 28, 44], is employed to solve pressure and velocity in RRM. A well documented disadvantage of CVFEM is fluid smearing or numerical dispersion between adjacent elements with distinct petrophysical properties and high order methods have been developed to reduce the smearing effect [1, 19, 23, 32, 52].

The linear equation system for pressure is solved by an efficient algebraic multigrid (AMG) method [63] available in SAMG [26] or HYPRE [4]. Then, TOF and TC are solved by the node-centred control/finite volume method in an efficient volume-by-volume manner after reordering the nodes. A tracing algorithm based on monotone edges is developed to reorder the nodes for situations involving non-Darcy edges where positive fluxes point from lower to higher pressure [75]. Based on TOF and TC, a range of quantities and dynamic proxies can be derived for flow diagnostics, such as dynamic Lorenz coefficient, sweep efficiency, and well allocation factors [45, 46].

Numerical well testing (NWT) is also termed geological well testing where numerical simulations are conducted on reservoir models to obtain well testing signals [11, 15, 40]. NWT has been applied to a range of reservoir problems. For example, [14] developed a geoengineering workflow based on NWT for correlating pressure transients of possible parameters to known geological features. Corbett et al. [13] systemically studied the effects of microporosity, macroporosity, and fracture porosity on pressure dissipation and their apparent homogenisation. Employing the geoengineering workflow, [20] studied the well test signals of naturally fractured reservoirs and explored the limitations of characteristic flow behaviours inherent to the double-porosity assumption. In these studies and applications of NWT, the pressure diffusivity equation is solved using commercial or open-source reservoir simulation software.

An alternative for NWT is to compute the diffusive time-of-flight (DTOF) of pressure perturbation front in petroleum reservoirs [18, 67, 68, 72]. DTOF can be regarded as a generalised concept of depth-of-investigation. The fast marching method (FMM) can be employed for computing DTOF efficiently on Cartesian grids to accelerate NWT [55, 59, 65]. However, it is difficult to preserve monotonicity in the solution by FMM on general unstructured meshes [56].

In this paper, an edge-based fast marching method with path correction (EFMMC) is developed to approximate DTOF efficiently on unstructured tetrahedral meshes. This allows us to estimate pressure transients, depth-of-investigation, and depletion efficiently in the RRM workflow. The combination of SBIM, flow diagnostics, and NWT allows for rapid prototyping and exploration of reservoir models. This is useful for choosing reliable models prior to detailed reservoir simulation, especially when there is no time or need for detailed reservoir simulation on a range of models.

This paper is organised as follows. First, flow diagnostics for unstructured meshes are reviewed. Second, an approximation method for NWT based on diffusive TOF on unstructured meshes is developed. Third, the implementation of both flow diagnostics and NWT for RRM is demonstrated. Fourth, the paper is concluded.

2 Review of flow diagnostics on unstructured grids

2.1 Governing equations for flow diagnostics

For flow diagnostics, the flow is assumed to be incompressible and steady-state [58]. The governing equations for pressure and velocity are

$$\mathbf{v} = -\lambda \nabla p \,, \tag{1}$$

$$\nabla \cdot \mathbf{v} = q \,, \tag{2}$$

where p is the flow potential that equals to $P - \rho g z$, P is absolute pressure, ρ is density, g is gravitational acceleration. Hereafter, p is simply referred to as pressure. λ is total mobility equal to $(k_{ro}/\mu_o + k_{rw}/\mu_w)K$ where K is the permeability tensor, k_{ro} and k_{rw} are the relative permeabilities of oil and water, and μ_o and μ_w are the viscosities of oil and water, respectively. $\mathbf{v}$ is total Darcy velocity and q is the volumetric source term. From Eqs. 1 and 2, we obtain the elliptic equation for pressure

$$-\nabla \cdot (\lambda \nabla p) = q \,. \tag{3}$$

The governing equations for time-of-flight (TOF) and tracer concentration (TC) in porous media are

$$\mathbf{v} \cdot \nabla \tau = \phi \,, \tag{4}$$

$$\mathbf{v} \cdot \nabla c = 0 \,, \tag{5}$$

where τ is TOF, c is TC, and ϕ is porosity. The two equations have the same hyperbolic advective transport form

$$\mathbf{v} \cdot \nabla u = b \,, \tag{6}$$

where u is TOF or TC and b is the corresponding source term. If $\nabla \cdot \mathbf{v} = 0$, Eq. 6 can be rewritten in the following form to help finite volume discretisation.

$$\nabla \cdot (\mathbf{v} u) = b \,. \tag{7}$$

Total velocity is in steady-state when well-rates and interactions among reservoir boundaries, such as faults and aquifer contacts, are constant. The controlled numerical experiment using a constant velocity field is a general feature of flow diagnostics [45] and is also employed in commercial software 3DSL [12]. In situations where transient effects (e.g. gravity segregation) are important for recovery, flow diagnostics are too simplistic, but still better than relying on the visualisation of static properties to compare and contrast reservoir models.

Flow diagnostics are not meant to replace a full-physics transient simulation but to provide dynamic proxies for ranking reservoir models prior to commencing more detailed reservoir simulation studies. For example, models associated with higher dynamic Lorenz coefficients tend to have greater sweep efficiency [45]. Flow diagnostics are particularly useful in situations where there is no time or need to run a full-physics detailed reservoir simulation to rank and compare a range of models [58].

2.2 Solution strategy for TOF and TC

The well-known control volume finite element method (CVFEM) [3, 42] is adopted for solving the elliptic equation for pressure in Eq. 3. Then velocity is obtained straightforwardly from Eq. 2 and applied to solve TOF and TC in Eqs. 4 and 5. Pressure is piecewise linear and velocity is piecewise constant in tetrahedral elements, while TOF and TC are piecewise constant in control volumes that are the dual of the tetrahedral elements. The details of the numerical method can be found in [75]. Here, we review the workflow, which is comprised of the following steps:

1. Solve Eq. 3 for pressure by use of CVFEM.
2. Obtain velocity for each tetrahedral element from Eq. 2.
3. Assemble fluxes between control volumes. An edge-based data structure is employed to store fluxes.

4. Solve Eq. 7 for TOF and TC by use of the control volume method, i.e. node-centred finite volume method.

In particular, we have developed an efficient monotone edge approach for solving TOF and TC efficiently volume-by-volume after reordering the nodes by DFS [75]. The control volume discretisation of Eq. 7 is

$$\sum_{j\in E_i} u_{ij}F_{ij} = b_i V_i \ , \tag{8}$$

where F_{ij} is the flux from control volume i to j, E_i is the set of all neighbouring nodes of node i, and u_{ij} is the value of u at the midpoint of edge ij. b is assumed to be constant in each control volume. Applying single-point upwind approximation for u_{ij} and mass conservation yields

$$u_i = \frac{\sum_{j\in E_i^U} u_j F_{ij}}{\sum_{j\in E_i^U} F_{ij}} - \frac{b_i V_i}{\sum_{j\in E_i^U} F_{ij}} \ , \tag{9}$$

where E_i^U and E_i^D are sets of upwind and downwind nodes for node i, respectively. TOF and TC could be solved volume-by-volume after being reordered by DFS [46]. However, there might be edges where positive F_{ij} points from lower to higher pressure, or in other words, where F_{ij} is against Darcy's law and is not monotone. These edges are termed non-Darcy edges while others are termed monotone edges. Non-Darcy edges lead to cycles in DFS and unknowns in a cycle need to be solved iteratively which is less efficient than volume-by-volume. The first and second terms on the right-hand-side of Eq. 9 are advection and source terms. Removing non-Darcy edges in the advection term, Eq. 9 is approximated by

$$u_i = \frac{\sum_{j\in \tilde{E}_i^U} u_j F_{ij}}{\sum_{j\in \tilde{E}_i^U} F_{ij}} - \frac{b_i V_i}{\sum_{j\in E_i^U} F_{ij}} \ , \tag{10}$$

where $\tilde{E}_i^U$ only contains nodes in E_i^U connected to node i by monotone edges. The source term in Eq. 10 remains the same as in Eq. 9. A reduced graph can be built by monotone edges. DFS on the reduced graph guarantees a sequence of nodes with no cycles. Then, the tracing algorithm (Eq. 10) can be applied locally node-by-node according to the sequence with all upwind nodes already computed. The solution is very close to that by solving Eq. 9 iteratively because the contribution to u_i from advection of non-Darcy edges is very low compared with that of monotone edges and the source term.

2.3 Derived quantities

TOF can help identify unswept volumes; TC visualises reservoir partitioning according to injectors or producers. In addition, a range of quantities, such as well-pair pore volume, well allocation factor, flow and storage capacity, dynamic Lorenz coefficient, sweep efficiency, and dimensionless time, can be derived straightforwardly from the solutions of TOF and TC for ranking reservoir models and development options in reservoir appraisal and development stages. The details of deriving these quantities can be found in [45, 58, 60, 75]. We have implemented the calculation of all these quantities in RRM.

3 An approximation method for numerical well testing on unstructured grids

3.1 Numerical well testing based on diffusive time-of-flight

Following [11, 13, 14, 20], the geoengineering workflow for integrated well testing comprises of (1) building reservoir prototypes of conceptual models from interpretations of the given outcrop or seismic data; (2) obtaining pressure transients by simulating draw-down or recovery for a range of possible properties and well locations; (3) analysing the numerical well test data; and (4) correlating the pressure transients to known geological features.

Efficient NWT is based on the diffusive time-of-flight (DTOF) of pressure front propagation for flows in porous media. The use of FMM to compute DTOF for propagation time, drainage volume, and pressure transients is reported in [59, 67, 68, 72]. The workflow of RRM can be accelerated by the application of SBIM for building reservoir models and EFMMC for computing pressure transients. The transient pressure solution for single-phase flow in porous media is governed by the diffusivity equation

$$\phi\mu c_t \frac{\partial p}{\partial t} = \nabla\cdot(K\nabla p) \ , \tag{11}$$

where p is pressure, K is the permeability tensor, c_t is total compressibility, μ is viscosity and ϕ is porosity. Using a Fourier transform and the asymptotic solution based on Eq. 11, it can be shown that the pressure front propagation in the high frequency limit is governed by the Eikonal equation [59, 65].

$$f|\nabla\tau| = 1 \ , \tag{12}$$

where f is the isotropic propagation speed. For anisotropic cases, the Eikonal equation can be written as [17]

$$\nabla\tau^T\cdot F^2\cdot\nabla\tau = 1 \ , \tag{13}$$

where τ is DTOF and F^2 is to square each element in F individually. The speed tensor F has entries

$$F_{ij} = \sqrt{\frac{K_{ij}}{\phi\mu c_t}} \ . \tag{14}$$

If K_{ij} is replaced by isotropic k, the expression for f is obtained. τ is related to the physical time t of pressure front propagation by

$$\tau = \sqrt{\beta t}\,, \tag{15}$$

where $\beta = 2, 4$ and 6 for 1D line, 2D radial, and 3D spherical flow patterns with homogeneous properties [72]. For cases with heterogeneous properties, t and β can be approximated by [73]

$$t = \left(\int_0^{\tau} \frac{d\tau'}{\sqrt{\beta(\tau')}}\right)^2\,, \tag{16}$$

$$\beta(\tau) = 2\frac{dlnV_p(\tau)}{dln\tau}\,, \tag{17}$$

where $V_p(\tau)$ denotes the drainage volume at τ.

The drainage volume at time t is denoted as $V(t)$ and can be computed numerically as the sum of all volumes with propagation time $\leq t$. For NWT, we assume that the Darcy flux is negligible outside the drainage volume and that reservoir pressure is approximated by a pseudo-steady-state solution. For all nodes affected by the pressure disturbance, the change of pressure with time satisfies [67]

$$\frac{\partial p}{\partial t} \approx -\frac{1}{c_t}\frac{q_w}{V(t)}\,, \tag{18}$$

where q_w is well flow rate. A key quantity in well testing is the pressure derivative Δp at the well defined and computed as [8]

$$\Delta p = -\frac{\partial p}{\partial ln(t)} \approx t\frac{1}{c_t}\frac{q_w}{V(t)}. \tag{19}$$

3.2 An edge-based fast marching method with path correction

The fast marching method (FMM) can be employed to solve Eq. 13 on Cartesian and nearly orthogonal corner-point grids [55]. However, FMM may yield unphysical results on unstructured tetrahedral meshes and an edge-based fast marching method (EFMMC) is developed here to approximate DTOF on unstructured meshes.

A review of FMM on structured and unstructured meshes is presented in the Appendix.

3.2.1 Homogeneous case

If F is homogeneous, we can compute the DTOF of each node semi-analytically. Figure 1 shows a simplified illustration in 2D. Let m be any node in the mesh and o be the boundary of propagation. The propagation time at o is zero. The characteristic curve is the straight line passing through o and m. The global speed profile is an ellipse centred at o with axes F_x and F_y. In 3D, the global speed profile is an ellipsoid centred at o with axes F_x, F_y, and F_z. Let c be the intersection point between the characteristic line and the speed ellipse or ellipsoid. The speed along the characteristic is $f_{om} = |\overrightarrow{oc}|$. Therefore, the analytical solution for τ at node m is

$$\tau_m^* = \frac{|\overrightarrow{om}|}{f_{om}}\,. \tag{20}$$

Applying Eq. 20 on all nodes or cells in the computational domain yields a semi-analytical solution. The validation of the semi-analytical method is presented in Section 3.3.1.

3.2.2 Heterogeneous case

Equation 12 is used on unstructured meshes with f denoting the magnitude of the anisotropic speed in the direction of propagation normal to the front. The key idea is to construct local speed profiles as shown in Fig. 2 for a 2D triangular element ijm. Suppose i is frozen, j and m are unfrozen and outside of the narrow band. Let the speed tensor F be $F = [F_x, 0; 0, F_y]$, neglecting the off-diagonal terms. The

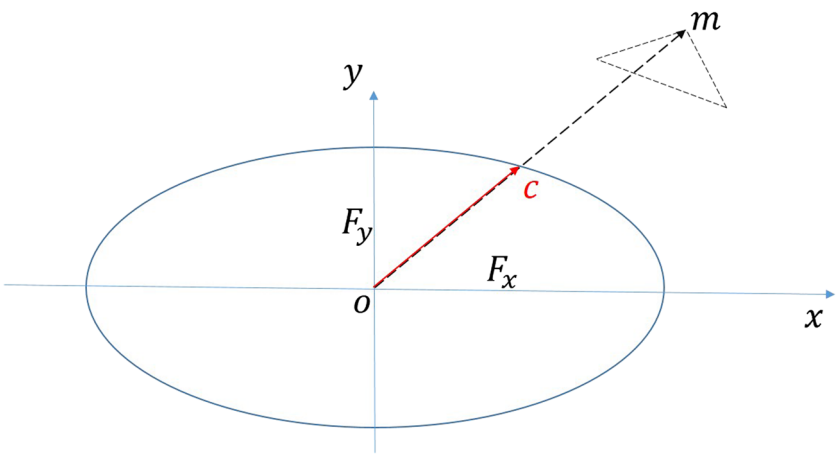

Fig. 1 Semi-analytical solution of the propagation time for an arbitrary node m in a 2D unstructured mesh. The global propagation speed tensor F is homogeneous and anisotropic. o is the boundary of propagation where the propagation time is zero. The characteristic curve is a line passing through o and m. The propagation speed along the characteristic is |**oc**|. Therefore, the semi-analytical solution of the propagation time at m is |**om**|/|**oc**|

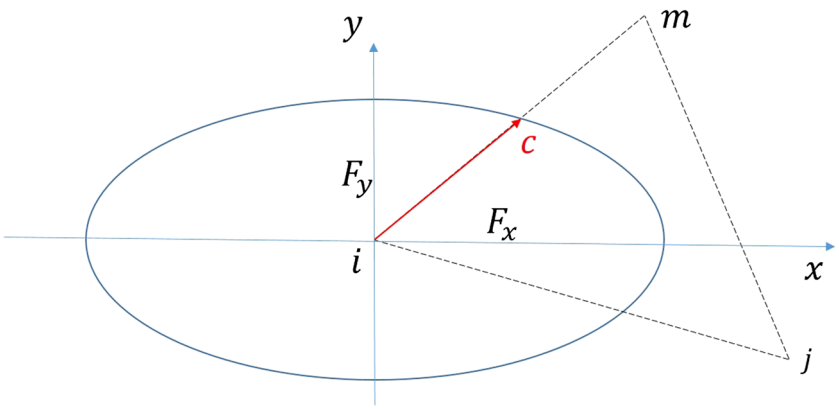

Fig. 2 Geometrical speed interpolation using anisotropic local speed tensor F at node i. The speed profile is an ellipse. Triangle ijm is an element in a 2D unstructured mesh. Node c is the intersection point between the ellipse and the line passing through i and m. The speed along edge im is equal to $|\mathbf{ic}|$. This plot only shows one possibility where $|\mathbf{ic}| < |\mathbf{im}|$. It is also possible that $|\mathbf{ic}| > |\mathbf{im}|$

local speed profile around node i is an ellipse [73] with axes F_x and F_y, described as

$$\frac{(x-x_i)^2}{F_x^2} + \frac{(y-y_i)^2}{F_y^2} = 1\,. \tag{21}$$

Let the coordinates of m be (x_m, y_m). The line passing i and m is

$$y - y_i = \frac{y_m - y_i}{x_m - x_i}(x - x_i)\,. \tag{22}$$

The coordinates of the common node c can be obtained by combining Eqs. 21 and 22. Then, the speed along edge im is simply $f_{im} = |\overrightarrow{ic}| > 0$.

The extension to 3D tetrahedral meshes is straightforward by constructing a 3D speed profile that is an ellipsoid. Let the speed tensor $F = [F_x, 0, 0; 0, F_y, 0; 0, 0, F_z]$; the speed ellipsoid is given by

$$\frac{(x-x_i)^2}{F_x^2} + \frac{(y-y_i)^2}{F_y^2} + \frac{(z-z_i)^2}{F_z^2} = 1\,. \tag{23}$$

The 3D line passing through i and m becomes

$$y - y_i = \frac{y_m - y_i}{x_m - x_i}(x - x_i)\,, \tag{24}$$

$$z - z_i = \frac{z_m - z_i}{x_m - x_i}(x - x_i)\,. \tag{25}$$

The speed f_{im} along edge im of a tetrahedral element can be obtained similarly as in 2D by combining the ellipsoid and line functions in Eqs. 23, 24, and 25; we obtain

$$\tau_m = \tau_i + \frac{|\overrightarrow{im}|}{f_{im}}\,, \tag{26}$$

where τ_m and τ_i are the propagation time at nodes m and i, respectively. The solution is guaranteed to be monotone since $f_{im} > 0$. As soon as a vertex becomes frozen, all unfrozen neighbouring nodes are computed and moved to the narrow band. If a neighbour is already in the narrow band, it is recomputed using the recently frozen vertex. The minimum of the old and new τ is adopted. This is different from FMM on Cartesian grids [55] where the new propagation time of a cell in the narrow band is obtained using a quadratic equation involving all frozen neighbouring cells.

The main source of error for the solution using Eq. 26 is that the path to a node through the edges is usually different from the path along the characteristic curve. In a homogeneous model, this error can be quantified as

$$\alpha = \tau_m^*/\tau_m\,, \tag{27}$$

where τ_m^* and τ_m are the semi-analytical and numerical solutions by Eqs. 20 and 26, respectively.

Assuming α is similar for homogeneous and heterogeneous models, we can approximate τ by $\alpha\tau_m$. If the path correction calculation is not included, the edge-based fast marching method will generate larger time-of-flight values, which is not the case with path correction. We will show in the test cases that this assumption is valid for unstructured meshes of approximately homogeneous mesh resolution. On the other hand, if the high- and low-propagation-speed regions have a high contrast in mesh resolution, the approximation becomes less accurate.

3.3 Validation examples

3.3.1 Box example with homogeneous propagation velocity tensors

For examples with homogeneous propagation speed, EFMMC is equivalent to the semi-analytical method. In this example, we compare FMM on Cartesian grids with the semi-analytical method. The model is a 100 m × 100 m × 100 m box. The boundary of propagation where $t = 0$ is at (0, 0, 0). The isotropic propagation speed is $f = 1$ m/s, while the anisotropic speed tensor has $F_x = F_y = 1$ and $F_z = 0.5$ m/s, neglecting the off-diagonal terms. Both f and F are homogeneous. A series of Cartesian grids with increasing resolution are built such that the first cell is centred at (0, 0, 0), since the propagation time t is defined on cell centres in Eqs. 31 and 32.

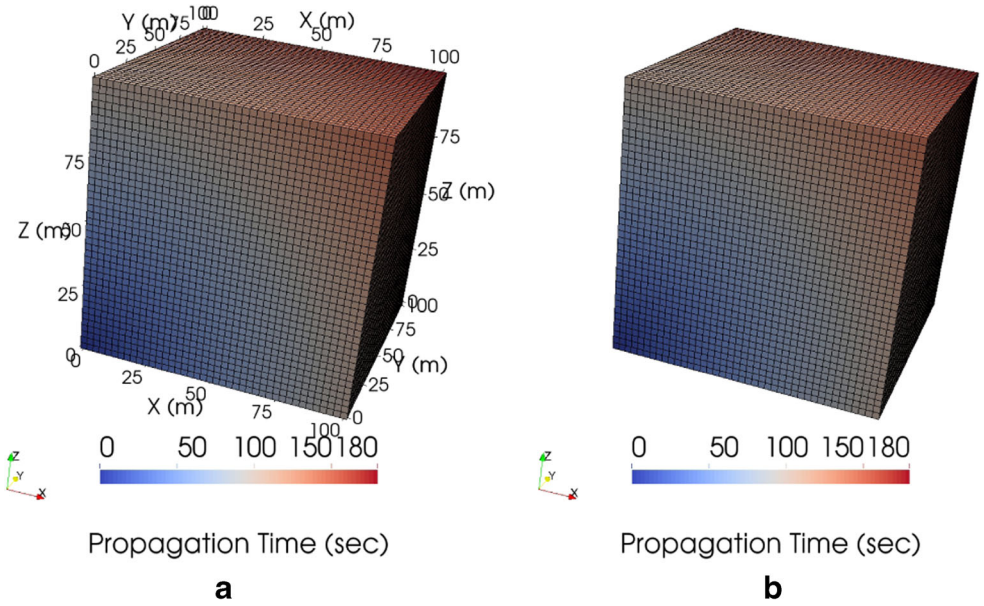

Fig. 3 Simulated propagation times using a homogeneous isotropic speed $f = 1$ m/s computed by FMM on a Cartesian grid (**a**) and the corresponding semi-analytical solution (**b**) for the box example of dimension 100 m × 100 m × 100 m. The propagation starts from (0, 0, 0)

The propagation time for isotropic speed f is computed numerically by FMM on a 41 × 41 × 41 Cartesian grid (Fig. 3a). The propagation time arithmetically averaged over all cells is 99.82 s, with a maximum time of 178.58 s at (100, 100, 100) m. The semi-analytical propagation time field (Fig. 3b) is very close to Fig. 3a. The average time is 96.53 s with a maximum of 173.21 s. The difference between the average propagation time computed semi-analytically and that numerically by FMM converges proportionally to the number of cells (Fig. 4).

Next, the anisotropic speed tensor F is used. The propagation time is computed by FMM on a 41 × 41 × 41 Cartesian grid (Fig. 5a), with an average of 137.94 s and a maximum of 250.87 s. The semi-analytical solution (Fig. 5b) has an average of 134.05 s and a maximum of 244.95 s. The difference between the average propagation time computed semi-analytically and that numerically by FMM converges proportionally to the number of cells (Fig. 6).

3.3.2 Heterogeneous example

In this test case, we test EFMMC for an idealised heterogeneous geological reservoir with large horizontal dimensions. The purpose of this reservoir model is not to represent a specific case study but to show that EFMMC is able to simulate changes in the pressure transient due to the presence of geological heterogeneity and reservoir

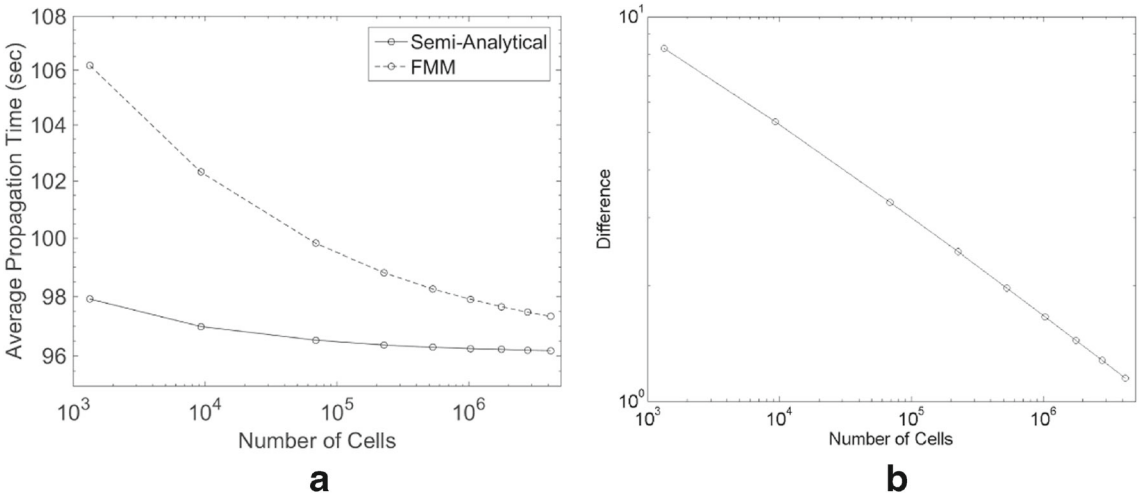

Fig. 4 Convergence of the average propagation time for the box example with a homogeneous isotropic speed $f = 1$ m/s obtained semi-analytically and numerically by FMM on a series of Cartesian grids with increasing resolution (**a**). Convergence of the difference between average propagation times by the semi-analytical method and FMM (**b**)

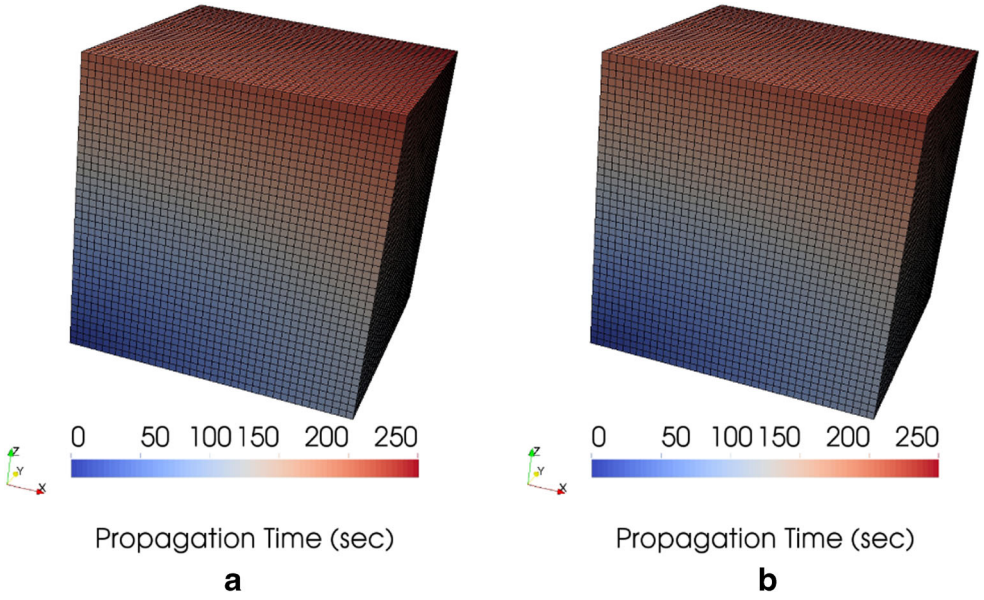

Fig. 5 Simulated propagation times using a homogeneous anisotropic speed tensor $F = (F_x, 0, 0; 0, F_y, 0; 0, 0, F_z) = (1, 0, 0; 0, 1, 0; 0, 0, 0.5)$ m/s computed by FMM on a Cartesian grid (**a**) and semi-analytically (**b**) for the box example of dimension 100 m × 100 m × 100 m. The propagation starts from (0, 0, 0)

boundaries. The model is a 1000 m × 1000 m × 40 m cuboid (Fig. 7a). The high-permeability region has $K_x = K_y = 200$ and $K_z = 2$ mD, while the low-permeability region has $K_x = K_y = 2$ and $K_z = 0.5$ mD. Viscosity $\mu = 1$ cp, porosity $\phi = 0.1$, and total compressibility $c_t = 10^{-5}$ psi^{-1} are all homogeneous. The propagation boundary where $\tau = 0$ is at $(0, 0, 0)$. It is obvious that low-permeability regions have higher τ (Fig. 7b). The new EFMMC is robust regarding skewed elements (Fig. 8).

The grid convergence of the average DTOF on unstructured tetrahedral meshes is not as stable as that on structured tetrahedral meshes (Fig. 9) due to the fact that unstructured meshes of different resolutions are not exactly of the same quality. However, the average DTOF on unstructured tetrahedral meshes is always between those computed on structured tetrahedral meshes and Cartesian meshes. The convergence study validates the accuracy of EFMMC on tetrahedral meshes.

3.3.3 Numerical well testing

The model is 1000 m × 1000 m × 40 m. A vertical producing well modelled as a line of nodes is placed in the centre of the reservoir that penetrates the entire formation.

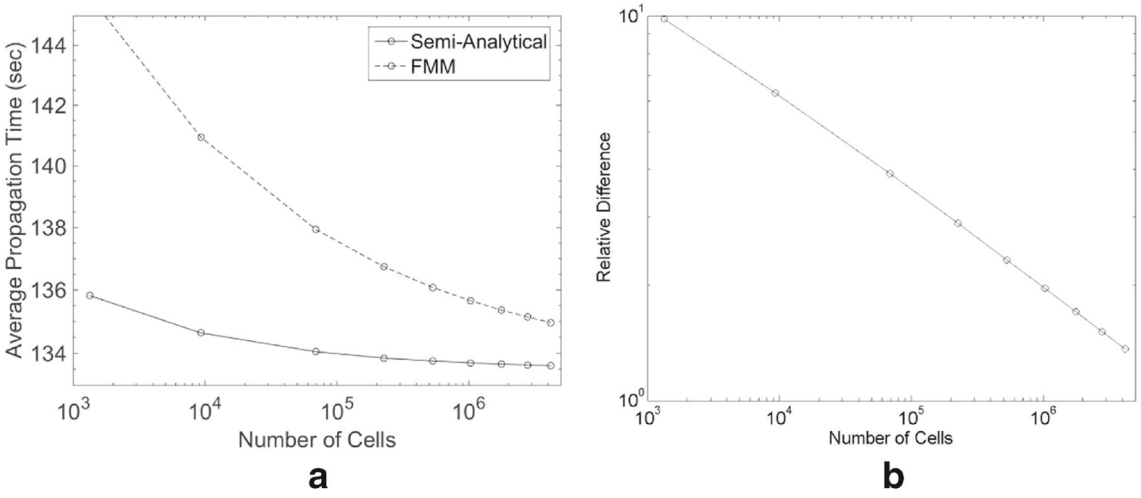

Fig. 6 Convergence of the average propagation time for the box example with a homogeneous anisotropic speed tensor $F = (F_x, 0, 0; 0, F_y, 0; 0, 0, F_z) = (1, 0, 0; 0, 1, 0; 0, 0, 0.5)$ m/s obtained semi-analytically and numerically by FMM on a series of Cartesian grids with increasing resolution (**a**). Convergence of the difference between average propagation times by the semi-analytical method and FMM (**b**)

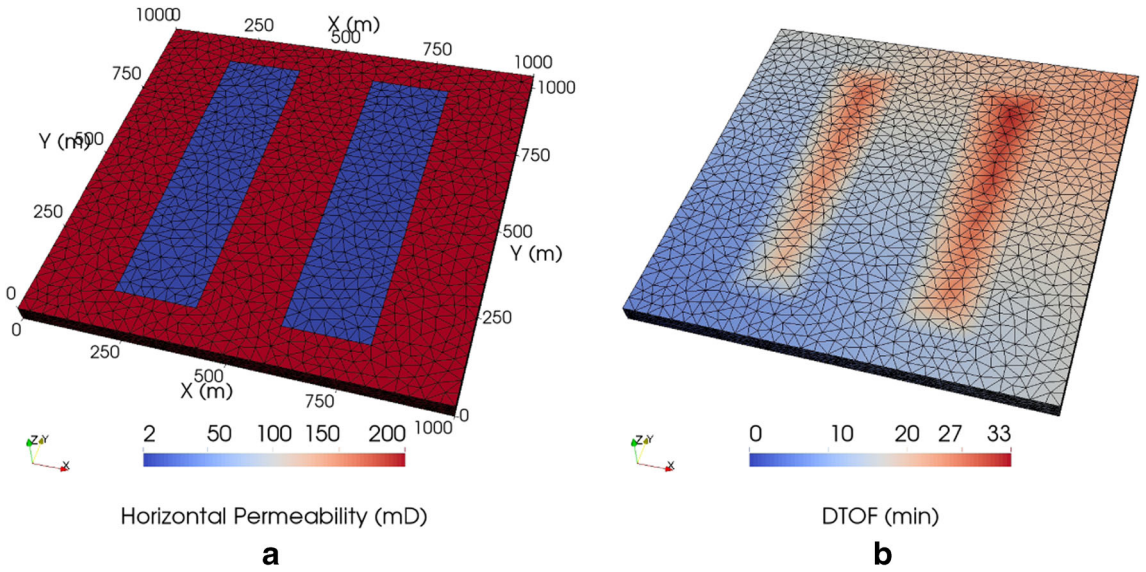

Fig. 7 The horizontal permeability field (**a**) and the DTOF field (**b**) using EFMMC on a fully unstructured tetrahedral mesh for the heterogeneous reservoir model of dimensions 1000 m × 1000 m × 40 m

The pressure disturbance propagates from the well. The production rate is assumed equivalent to $q_w = 10$ rb/day where rb stands for reservoir barrel.

Firstly, the reservoir is assumed to be homogeneous with a permeability $K_x = K_y = K_z = 0.01$ mD, porosity $\phi = 0.1$, total compressibility $c_t = 3 \times 10^{-4}$ psi^{-1} and fluid viscosity $\mu = 0.02$ cp. Figure 10 shows the propagation time t computed using EFMMC on an unstructured tetrahedral mesh that is locally refined near the well. The front propagates radially from the well towards the boundary.

From Fig. 10, we can calculate the drainage volume numerically at time t, denoted as $V(t)$, as the sum of all volumes with propagation time $\leq t$. Figure 11 compares $V(t)$ with the analytical solution for an infinite acting drainage volume $V^*(t)$ given by [67]

$$V^*(t) = \pi r^2 h\phi = \frac{4\phi k h t}{\mu c_t}, \tag{28}$$

where k is the homogeneous isotropic permeability and r the distance to the well. $V(t)$ and $V^*(t)$ overlap until the

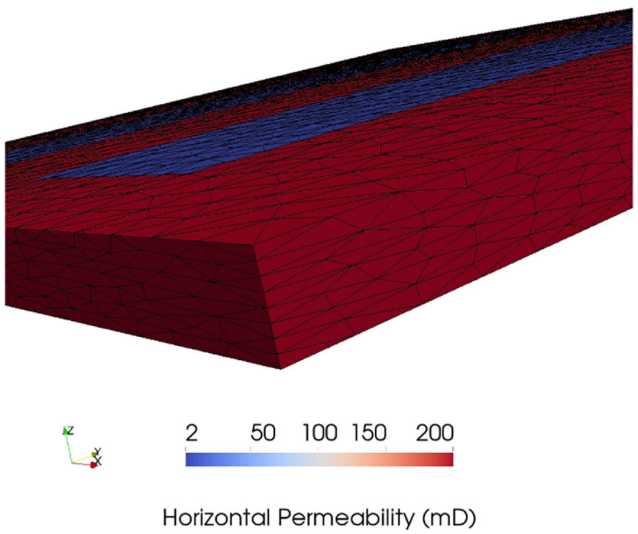

Fig. 8 A close-up side view of the highly skewed tetrahedral elements in the heterogeneous reservoir model

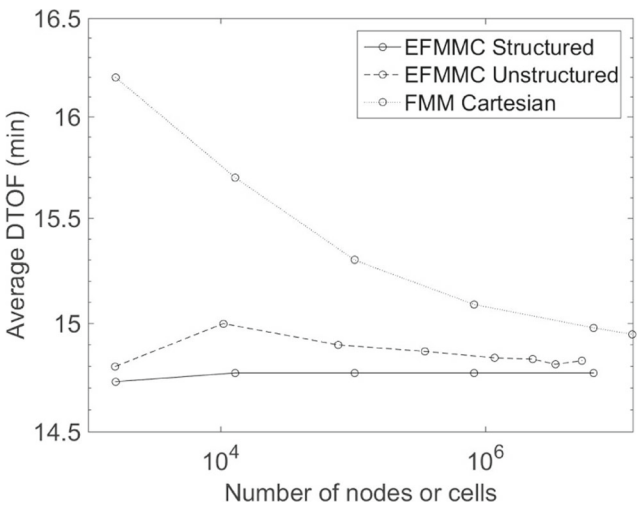

Fig. 9 Convergence of the average DTOF for the heterogeneous reservoir model computed using EFMMC on structured tetrahedral meshes, EFMMC on unstructured tetrahedral meshes and FMM on Cartesian grids. Structured tetrahedral meshes are created by splitting Cartesian grids into tetrahedrons rather than using a dedicated meshing software. The tetrahedrons have a structure so the mesh is termed structured tetrahedral mesh

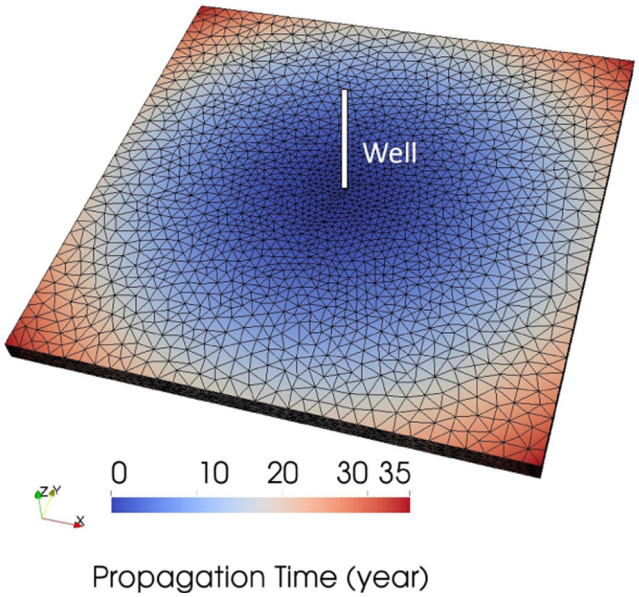

Fig. 10 Plot of pressure front propagation times away from the centrally located well for a homogeneous reservoir using EFMMC. The unstructured tetrahedral mesh is locally refined near the well. As expected, the propagation is almost radial

pressure front reaches no-flow boundaries (Fig. 11). The slope of the curve for $V(t)$ becomes zero after the entire reservoir has been drained.

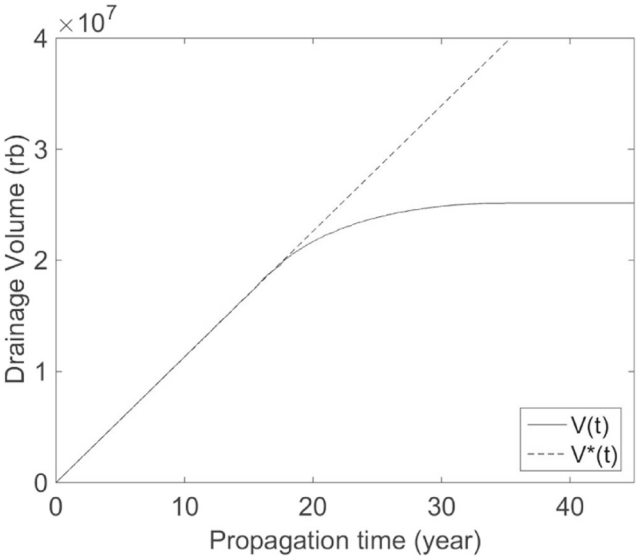

Fig. 11 Drainage volume as a function of time computed using EFMMC on an unstructured tetrahedral mesh compared with the analytical solution for an infinite acting reservoir. The two curves overlap until the no-flow boundaries are reached. The slope of the solid curve becomes zero after the entire reservoir has been drained

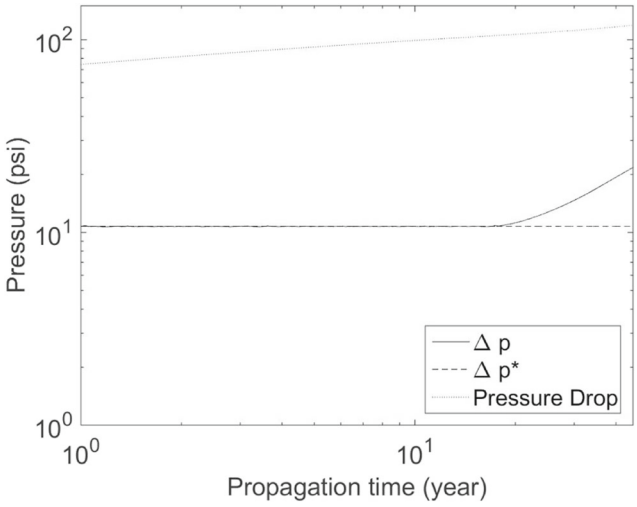

Fig. 12 Pressure derivative, a key diagnostic in well testing, as a function of time computed by EFMMC on an unstructured tetrahedral mesh compared with the analytical solution for an infinite acting reservoir. The two curves overlap until the no-flow boundaries are reached

Figure 12 plots Δp as a function of time at the well. The analytical solution for an infinite acting reservoir is

$$\Delta p^* = \frac{q_w \mu}{4\phi k h}, \tag{29}$$

obtained by substituting Eq. (28) into Eq. (19). The two curves overlap until the no-flow boundaries are reached.

Next, a heterogeneous reservoir is assumed. As with the heterogeneous reservoir depicted in Fig. 7, the reservoir model is highly idealised and does not represent a specific case study. Its purpose is to demonstrate that EFMMC is able to calculate pressure transients that capture geological heterogeneity and boundary conditions. The well location and production rate are unchanged. The high-permeability region has $K_x = K_y = K_z = 100$ mD, while the low-permeability regions have $K_x = K_y = K_z = 10$ mD (Fig. 13a). Porosity $\phi = 0.1$, total compressibility $c_t = 3 \times 10^{-4}$ psi^{-1} and fluid viscosity $\mu = 0.02$ cp are homogeneous. Figure 13b presents the propagation time.

For pressure transient analysis, we can record the change of Δp^* with time at the well (Fig. 14). The changes in the slope of the derivative curves indicate different propagation patterns due to the presence of geological heterogeneity and no-flow boundaries. For validation, the curve obtained by EFMMC on unstructured tetrahedral mesh is compared with that by FMM on Cartesian grid [67]. The two curves indicate similar flow patterns. The comparison of FMM on Cartesian grids with commercial simulators has been discussed in [68, 69].

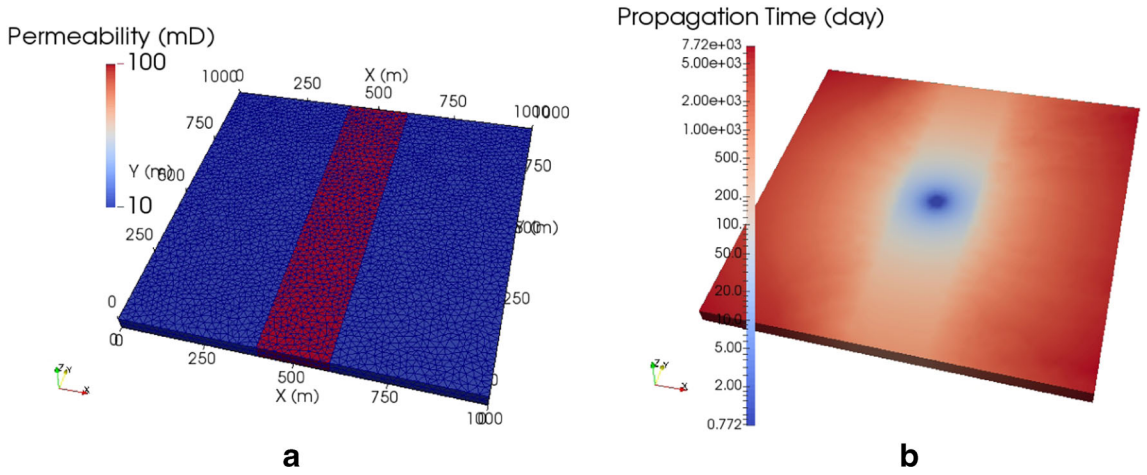

Fig. 13 Permeability field (**a**) and resulting propagation time (**b**) computed by EFMMC on a fully unstructured tetrahedral mesh for a heterogeneous reservoir. The mesh resolution is approximately homogeneous to improve numerical accuracy. There are 10639 nodes and 46432 tetrahedral elements

There are four phases in the evolution of the pressure derivative. The first phase is an infinite acting period (< 30 days). The pressure front propagates radially while neither the low-permeability regions nor the no-flow boundaries are reached. The second phase is from 30 days to around 700 days. Here the pressure propagation is affected by the low-permeability regions and propagates mainly linearly along $+y$ and $-y$ directions. The third phase is from 700 to 6000 days. Here the pressure front has reached the boundaries at $y = 0$ and 1000 m and is mainly propagating in the low-permeability regions. The fourth phase is after 6000 days when the pressure front reaches the no-flow boundaries at $x = 0$ and 1000 m. The change of drainage volume with time is plotted in Fig. 15, which also indicate four flow regimes. It is clear that the drainage volume stays almost constant, reflecting that the pressure front has reached the no-flow boundaries.

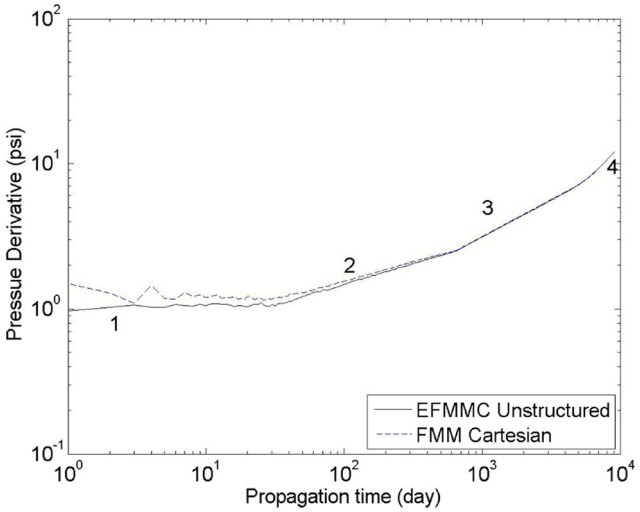

Fig. 14 Pressure derivative as a function of time computed by EFMMC on the unstructured tetrahedral mesh in Fig. 13a and by FMM on a $101 \times 101 \times 1$ Cartesian grid. The number of nodes in the unstructured mesh is close to the number of cells in the Cartesian grid

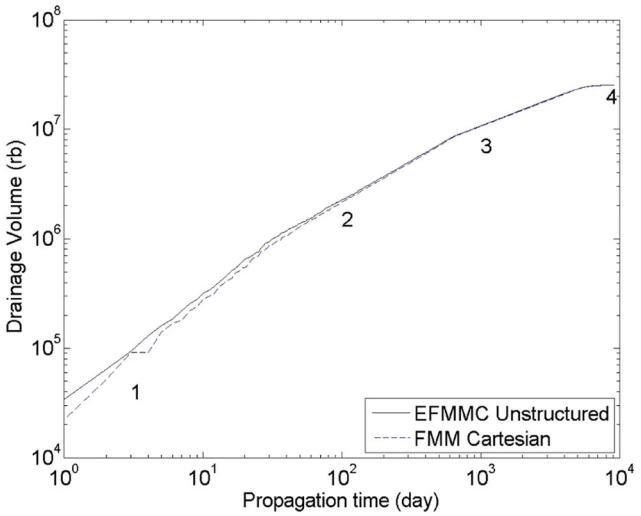

Fig. 15 Drainage volume as a function of time computed by EFMMC on the unstructured tetrahedral mesh in Fig. 13a and by FMM on a $101 \times 101 \times 1$ Cartesian grid. The number of nodes in the unstructured mesh is close to the number of cells in the Cartesian grid

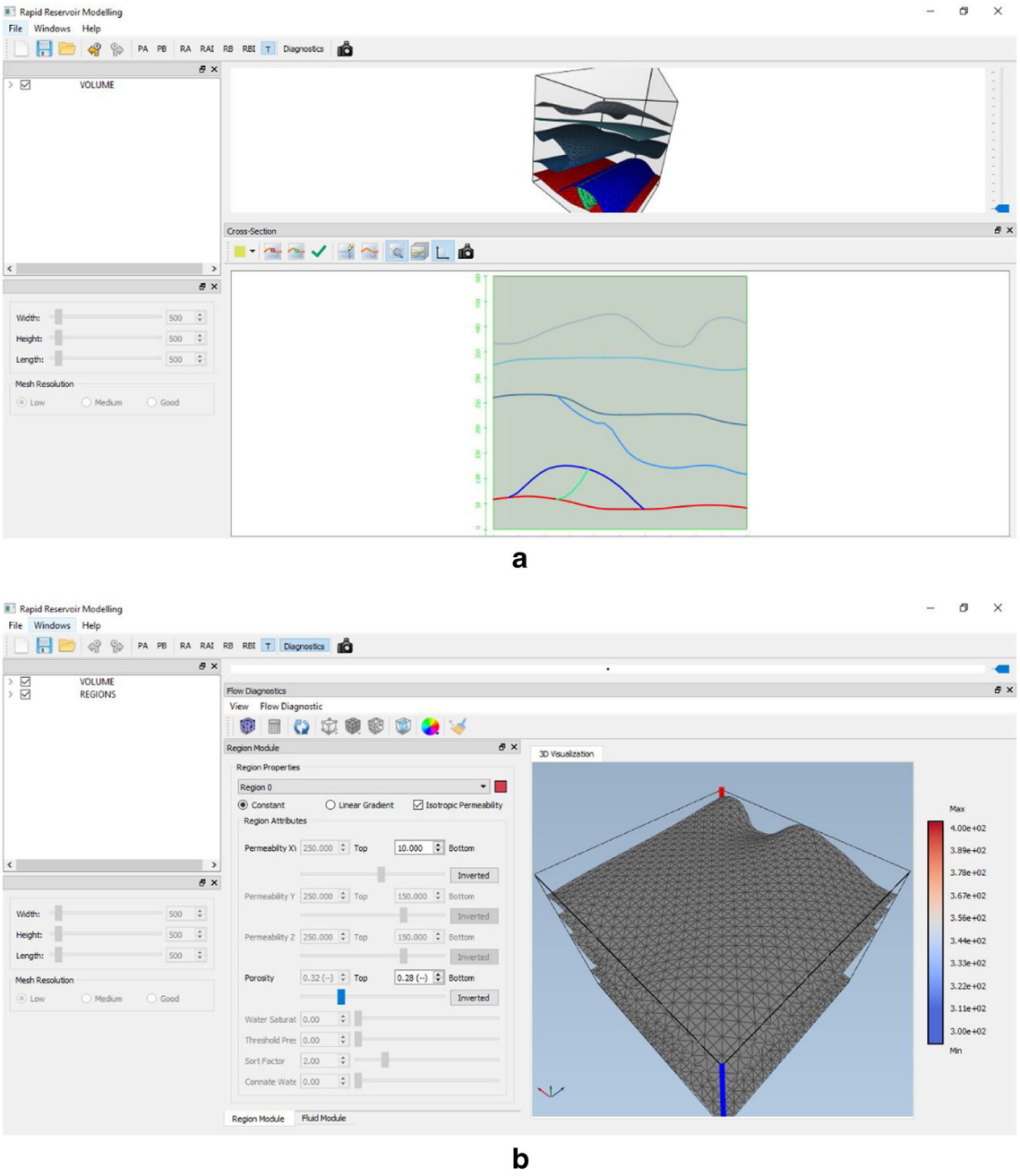

Fig. 16 Sketch-based interface modelling in RRM where curves are sketched on 2D cross sections to build a 3D model (**a**). Flow diagnostics window with a surface 4–8 mesh (**b**)

4 Implementation in RRM prototype

This paper does not present the first time that RRM has been implemented and earlier, more limited RRM developments have been discussed in [31, 74, 75]. An idealised surface-based model representing a series of stacked channelised sandbodies is sketched (Fig. 16a) to demonstrate the flexibility of our workflow but not to show a specific case study. In SBIM, a surface can be created by sketching on multiple cross-sections or by 3D extrusion. The sketching is scale independent so that models at basin, reservoir, inter-well, or outcrop scales can all be created. Surfaces represent the inner boundaries between different regions (e.g. sandbodies) in the conceptual reservoir. Outer

boundaries include the top and bottom sketched surfaces as well as the four vertical boundaries of the sketching domain. The heterogeneous model is idealised and only serves to show that the algorithm leads to pressure derivatives and drainage volume calculations that account for geological heterogeneity and boundary conditions.

Four to eight meshes [66] are generated on the surfaces (Fig. 16b). Four to eight meshes are employed because of their ease of generation, but other types of triangular meshes could also be used in principle to represent the surfaces. Unstructured triangular meshes are generated on the four vertical outer boundaries adapting to all intersecting curves of the sketched surfaces. Then, a surface mesh is created by joining the triangular meshes on all surfaces. Based on the surface mesh, an unstructured tetrahedral mesh is generated by TetGen. Other mesh generators could also be used but we employ TetGen here. In TetGen, extra points might be added on the surface for improving the quality of tetrahedral elements [61]. The volume mesh adapts to the surfaces in the sense that every surface can be described by connected facets of the tetrahedral elements. In RRM, all steps of mesh generation are integrated and automatically completed.

We demonstrate the implementation of NWT and flow diagnostics in RRM for comparing potential well locations. Permeability is isotropic and heterogeneous (Fig. 17). Porosity for each region is set to be 0.28. The total pore volume of this model is about 150 million reservoir barrels.

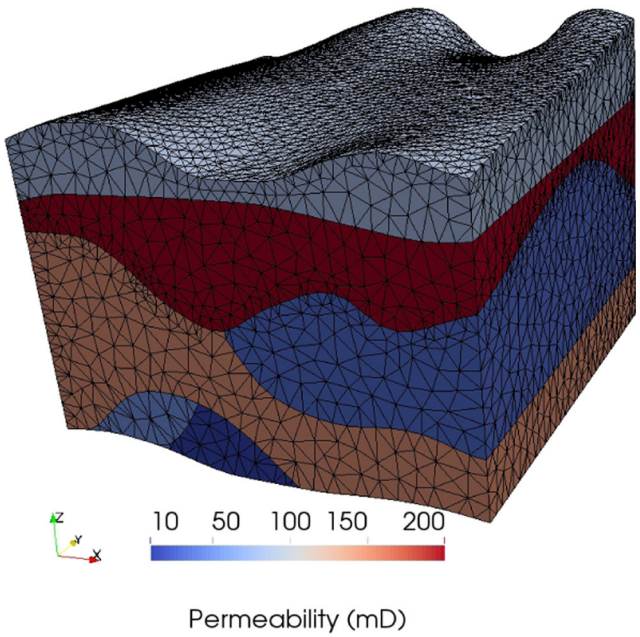

Fig. 17 Permeability distribution for the model and the unstructured tetrahedral mesh that adapts to all surfaces

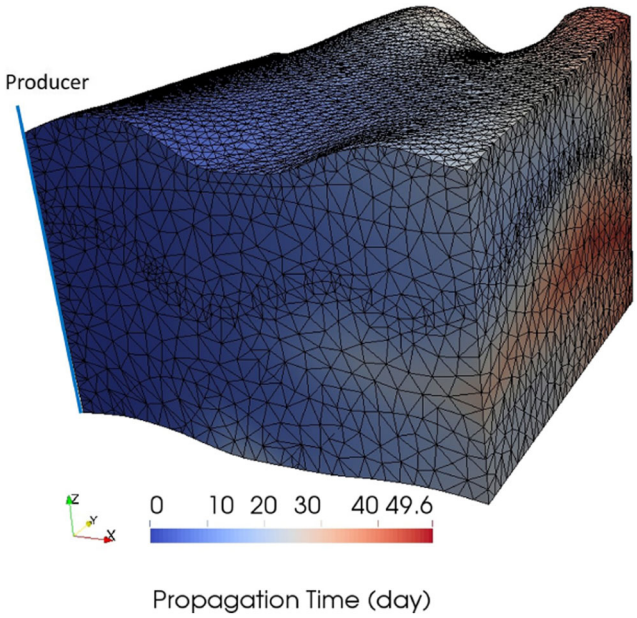

Fig. 18 Propagation time of pressure perturbation front in the heterogeneous surface-based reservoir model

For numerical well testing, flow is single-phase with viscosity 1 cP and total compressibility 1×10^{-4} psi^{-1}. A rate-controlled producer is implemented (Fig. 18). The well rate is 10 rb/day. Recall that the model is idealised and only serves to show the RRM functionality. By qualitative observation, we see that most of the reservoir is drained before 30 days (Fig. 18). Here we call a volume is drained if it is reached by the pressure perturbation and starts to be produced. From the drainage volume plot, we see that approximately all volumes are drained at the time between 40 and 50 days (Fig. 19). However, the slope of the drainage volume curve starts to decrease much earlier. From the pressure derivative plot, it is clear that the slope of derivative increases considerably at around 18 days when reservoir boundaries have been reached and the flow enters the pseudo-steady-state (PSS) stage. Areas of propagation time > 18 days start to be drained and all volumes are drained at about 49 days. Before 18 days, the impact of permeability heterogeneity is seen as small-scale fluctuations in the pressure derivative curve. The result is approximate as there are numerical errors due to EFMMC and the transformation from diffusive TOF to physical time; however, the result still yields a good approximation of the reservoir dynamics.

Then, a new scenario is modelled where the location of the producer is changed (Fig. 20). The propagation time of the pressure perturbation front is recalculated (Fig. 20). The pressure derivative and evolution of drainge volumes

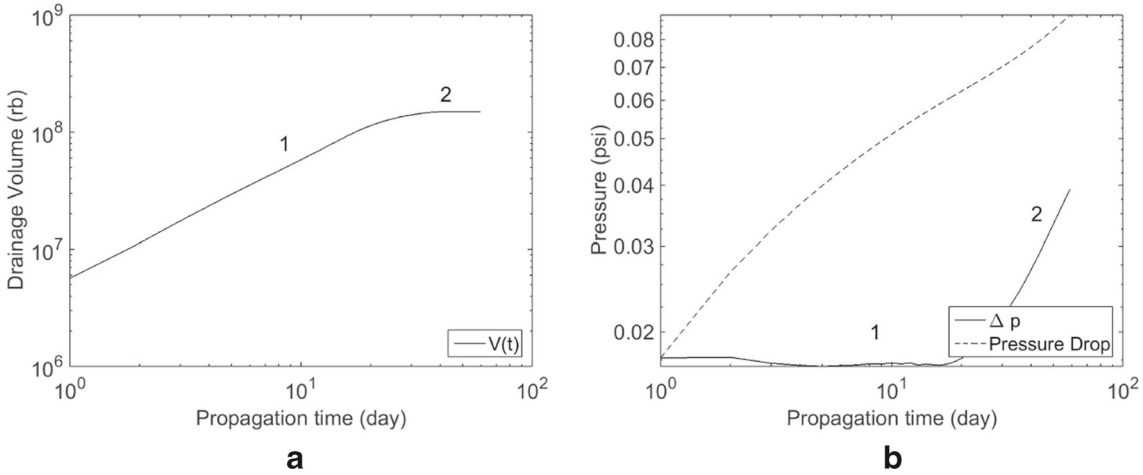

Fig. 19 Drainage volume (**a**) and pressure drop and pressure derivative (**b**) over propagation time in the heterogeneous model

show three distinct behaviours (Fig. 21). The first stage is radial infinite acting which is characterised by a line of approximately zero slope. In the second stage, the pressure perturbation reaches one of the reservoir boundaries at around 5 days and the curve has a positive slope. In the third stage, the slope becomes steeper and all reservoir boundaries have been reached. Between the second and third stages, the change of slope is gradual from when all reservoir boundaries are reached at around 25 days until all volumes are drained at about 36.5 days, seen clearly from Fig. 20. The flow is close to PSS at around 5 days. If an earlier flow regime close to PSS is desirable, the well location in Fig. 20 is preferred over that in Fig. 18 in this idealised example.

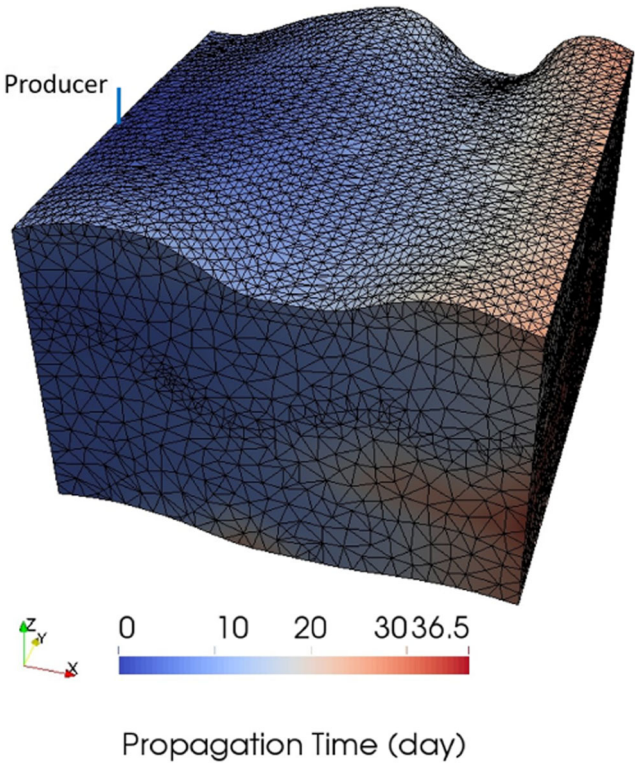

Fig. 20 Propagation time of pressure perturbation front in the heterogeneous surface-based reservoir model with a different producer location (compare with Fig. 18)

For completeness of the workflow, we further demonstrate the flow diagnostics functionality. The purpose is to demonstrate the integrated workflow, not to discuss specific case studies. The comparison of flow diagnostics with commercial simulators has been discussed by [45, 62]. Flow is assumed to be incompressible. An injector well and a producer well are assumed to be vertical and penetrate the entire model. The well pattern is quarter five-spot. Well-block pressure values are set on both wells directly as Dirichlet boundary conditions. The continuous pressure field indicates that all regions are fully connected (Fig. 22a). The solution of forward TOF represents the travel time from the injector (Fig. 22b). As porosity is homogeneous, the influence of permeability heterogeneity on forward TOF is clearly seen. There is only one injector and one producer, so the tracer concentration of all nodes associated with either the injector or producer is one.

The flow capacity over storage capacity diagram is derived based on TOF solutions (Fig. 23a). The reference solutions are for a homogeneous model and displacement,

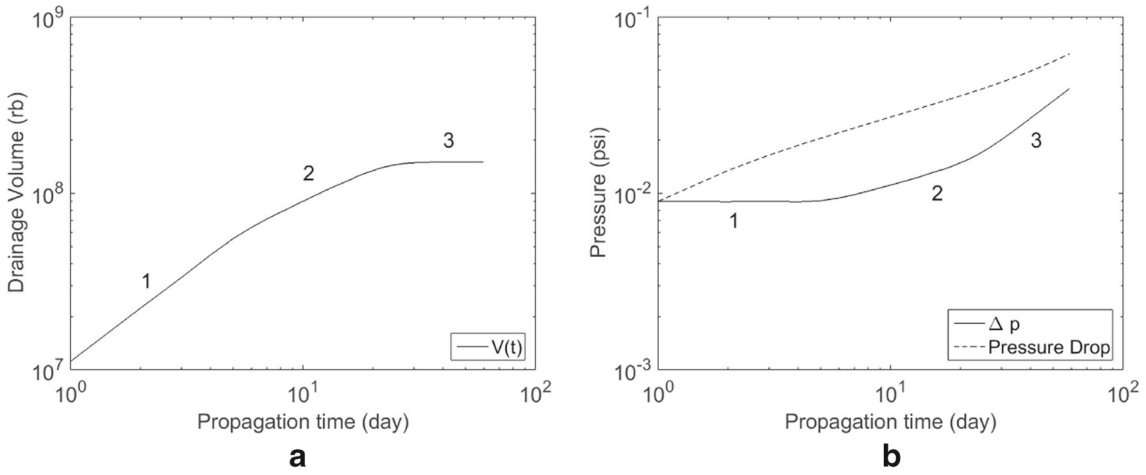

Fig. 21 Drainage volume (**a**) and pressure drop and pressure derivative (**b**) over propagation time for modified well locations in the heterogeneous model

respectively. The homogeneous model is of the same geometry as the heterogeneous model but with homogeneous permeability 150 mD. Homogeneous displacement refers to 1D homogeneous piston-like displacement with zero residual oil saturation such that flow capacity is always equal to storage capacity [58, 75]. The dynamic Lorenz coefficient of the heterogeneous model is approximately 0.22. The reference values of homogeneous model and displacement are 0.16 and 0, respectively. Another derived quantity based on TOF is sweep efficiency versus dimensionless time (Fig. 23b). Water breakthrough is generally at dimensionless time equal to 1 when a homogeneous piston-like displacement has 100% sweep efficiency [45]. The sweep efficiency of the heterogeneous model at the time of water breakthrough is around 80%. This is consistent with the forward TOF, which is higher at some nodes near the corners

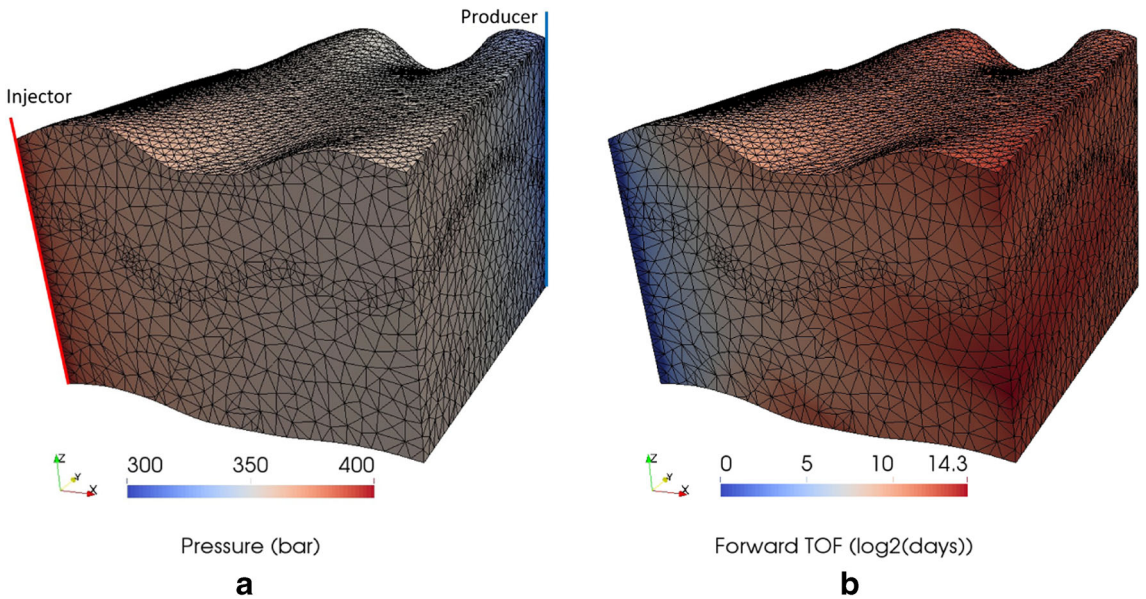

Fig. 22 Pressure (**a**) and forward time-of-flight (**b**) solution on the unstructured tetrahedral mesh for flow diagnostics. Forward time-of-flight is the travel time from the injector to each position in the model

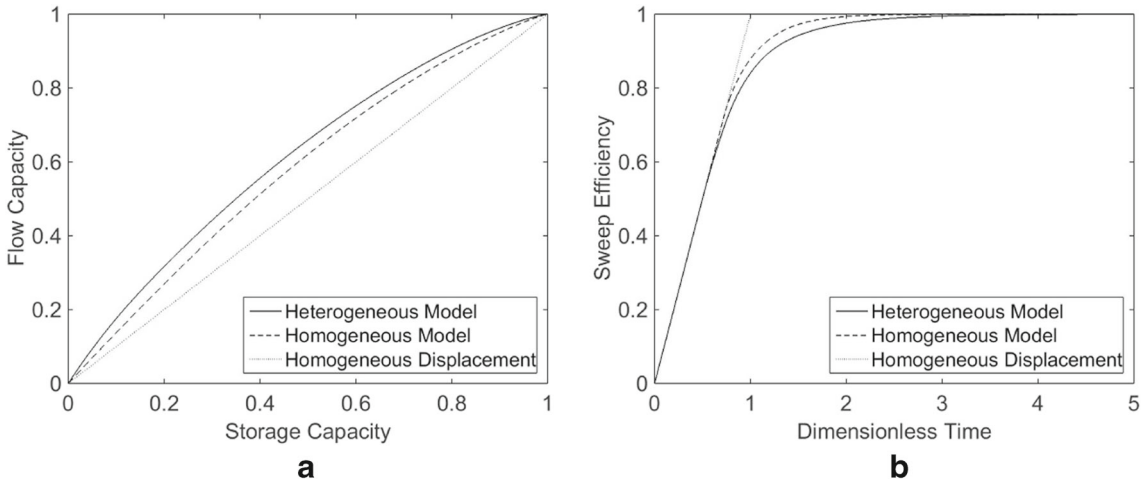

Fig. 23 Plots of flow capacity over storage capacity (**a**) and sweep efficiency over dimensionless time (**b**) for the heterogeneous surface-based reservoir model. The reference solutions are for a homogeneous model and displacement, respectively. The homogeneous model is of the same geometry as the heterogeneous model but with homogeneous properties

of the model than the TOF at the producer (Fig. 22b). The sweep efficiencies for homogeneous model and homogeneous displacement are 85% and 100%, respectively. Water breakthrough in the heterogeneous model occurs approximately three times faster before 100% recovery is reached (Fig. 23b).

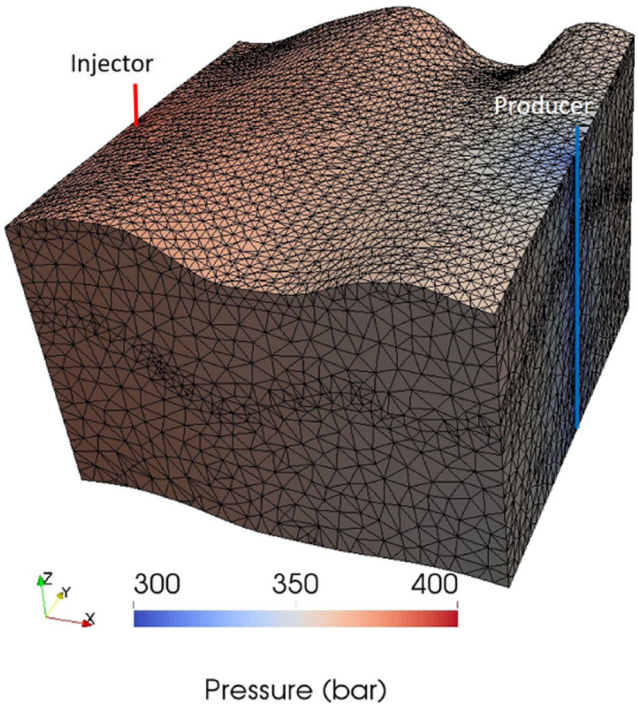

Fig. 24 Pressure solution of the heterogeneous surface-based model with modified well locations (compare with Fig. 22a)

Next, the two wells are moved to the centres of opposite boundary surfaces (Fig. 24). This is a new scenario to see how different well placements for the same geology impact flow. In RRM, wells can be moved in the model, but new meshes need to be generated to adapt to new well locations. As expected, the pressure distribution changes accordingly but is still smooth. The flow capacity over storage capacity curves for heterogeneous and homogeneous models (Fig. 25a) almost overlap with each other, influenced mainly by reservoir geometry and well locations. The dynamic Lorenz coefficients for heterogeneous and homogeneous models are now 0.255 and 0.243, respectively. The sweep efficiencies at water breakthrough for the heterogeneous and homogeneous models are both around 70% (Fig. 25b). Comparing Figs. 23 and 25 shows that generally the sweep efficiency decreases with higher heterogeneity quantified by the dynamic Lorenz coefficient. The well locations in Fig. 22a are preferred if higher sweep efficiency is desirable for production with water flood.

The total time needed for mesh generation, flow diagnostics, and numerical well testing in the demonstrated example is less than a minute on a normal desktop computer. We can hence quickly generate multiple geological scenarios to test how flow is impacted by geological heterogeneity and begin to compare, contrast, and rank reservoir models. All

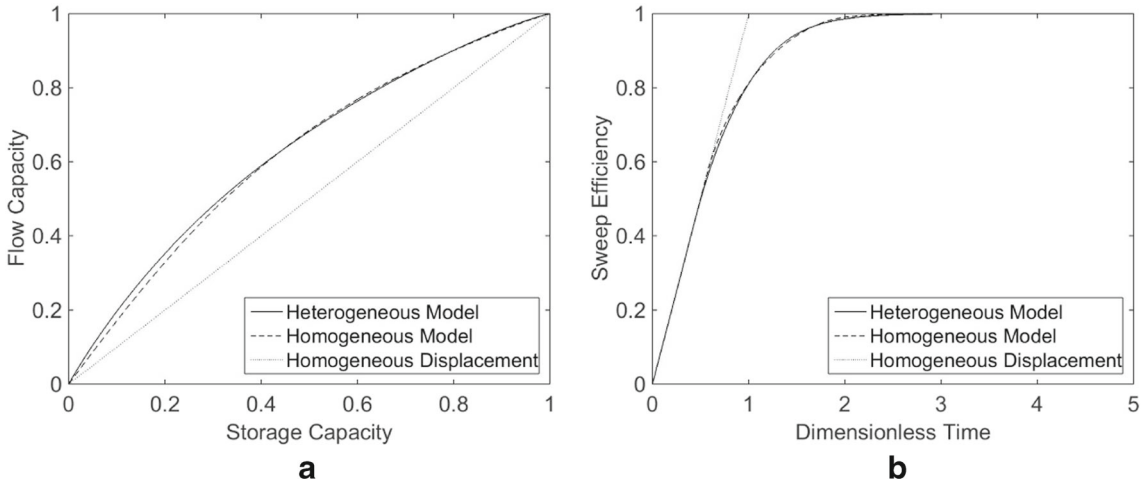

Fig. 25 Plots of flow capacity over storage capacity (**a**) and sweep efficiency over dimensionless time (**b**) for the heterogeneous surface-based reservoir model with modified well locations. The reference solutions are for a homogeneous model and displacement, respectively. The homogeneous model is of the same geometry as the heterogeneous model but with homogeneous properties

steps of flow diagnostics and numerical well testing are fully integrated and automatically executed.

5 Conclusions

An edge-based fast marching method with path correction (EFMMC) has been developed for approximating the diffusive TOF of pressure front propagation efficiently on unstructured tetrahedral meshes. In addition, a tracing algorithm for flow diagnostics has been reviewed. Based on these algorithms, we have implemented flow diagnostics and numerical well testing (NWT) on unstructured tetrahedral meshes for rapid reservoir modelling (RRM). It should be noted that these algorithms are not bound to the RRM workflow. They can be applied to other models involving unstructured tetrahedral meshes. The total computational cost of flow diagnostics and NWT and is less than seven minutes for models with one million nodes on a standard desktop PC. This paper demonstrates that an implementation of the workflow consisting of integrated sketch-based interface modelling, unstructured mesh generation, flow diagnostics, and numerical well testing is possible. The algorithms developed in this paper can be used for numerical well testing in reservoir models involving unstructured meshes.

Acknowledgements Sebastian Geiger thanks Energi Simulation for supporting his Chair in Carbonate Reservoir Simulation.

Funding information This research is funded by members of the Rapid Reservoir Modelling consortium (Equinor, ExxonMobil, Shell, Petrobras, and IBM Research/CAS Alberta).

Appendix: A review of fast marching methods for structured and unstructured grids

The fast marching method (FMM) is an efficient non-iterative algorithm developed by [55] to solve the boundary value problems of the Eikonal equation for monotonically advancing fronts. Here, monotonicity means that the front or interface can only expand or shrink. A number of practical applications have been modelled based on the principles of FMM. For example, [16] presented a characteristic FMM for wave propagation in a moving medium. Elias et al. [21] developed a FMM based on the finite element method for computing the distance field in computer graphics. Sermesant et al. [54] presented an anisotropic multi-front FMM for real-time simulation of cardiac electrophysiology. Sharifi et al. [59] used FMM to approximate the propagation time of pressure fronts of flows in porous media for reservoir characterisation. Zhang et al. [73] applied FMM to estimate drainage volumes and pressure depletion for numerical well testing in shale gas reservoirs. Zhang et al. [70] presented a scalable massively parallel implementation of FMM for large industrial models.

The FMM as presented in [55] is based on solving the Eikonal equation using upwind finite difference approximation. The method is efficient, consistent, and monotone on Cartesian grids with a computational complexity of $\mathcal{O}(N \log N)$ where N is the number of unknowns [35]. On unstructured meshes where the connectivity between elements are often not aligned with the main coordinate axes, the gradient in the Eikonal equation could be discretised based on directional derivatives along edges [56]. However,

this approach is not monotone. Thus, a causality condition is introduced to ensure that only monotone results are obtained. The causality condition requires that the computed propagation time on an unknown node must be higher than the propagation time on known nodes. But, it is possible that no neighbouring element satisfies the causality condition for a node in an unstructured mesh containing skewed elements. Sethian and Vladimirsky [56] suggest to solve this problem by splitting the obtuse angles and constructing virtual supportive triangles. The extension of this approach to 3D unstructured tetrahedral meshes, where skewed elements are more common, is rather cumbersome. An alternative solution can be defined for the Eikonal equation using the finite element method [21], although similar difficulties arise when fulfilling the causality condition.

Fast marching methods on Cartesian grids

FMM solves Eq. 12 numerically subject to boundary condition

$$t = g(\mathbf{x}) , \quad x \in \Gamma \tag{30}$$

where Γ is a subset of Ω. Both F and g are given, and the computation starts from Γ. Here we let $g(\mathbf{x}) = 0$ similarly as in [55]. For isotropic propagation speeds, the finite difference discretisation for Eq. 12 on 3D Cartesian grids is

$$\left(\frac{t_{ijk} - t^{*x}}{\Delta x}\right)^2 + \left(\frac{t_{ijk} - t^{*y}}{\Delta y}\right)^2 + \left(\frac{t_{ijk} - t^{*z}}{\Delta z}\right)^2 = \frac{1}{f^2} , \tag{31}$$

where t_{ijk} is the propagation arrival time of the cell with index (i, j, k). t^{*x}, t^{*y}, and t^{*z} are the upwind values along x, y, and z axes, respectively. For an anisotropic propagation speed tensor, Eq. 13 is discretised as [73]

$$\left(F_x \cdot \frac{t_{ijk} - t^{*x}}{\Delta x}\right)^2 + \left(F_y \cdot \frac{t_{ijk} - t^{*y}}{\Delta y}\right)^2 + \left(F_z \cdot \frac{t_{ijk} - t^{*z}}{\Delta z}\right)^2 = 1 , \tag{32}$$

where F_x, F_y, and F_z are the propagation speeds at cell (i, j, k) along x, y, and z directions, respectively. If the speed is isotropic ($F_x = F_y = F_z = f$), Eq. 32 is equal to Eq. 31. The steps of FMM for computing the propagation time on a Cartesian grid are summarised as follows [55]:

1. Label all boundary cells as frozen. These cells have $t = 0$.
2. Compute t for all cells that have at least one frozen neighbour and label them as candidate. All candidate cells form the narrow band [55]. Because of monotonicity, a cell can only have at most one frozen neighbour along a direction which is also the upwind cell. If there is no neighbour along a direction, then the corresponding term in Eq. 31 or 32 is simply neglected.
3. Find the cell with smallest t in the narrow band, mark it frozen, and remove it from narrow band.
4. Solve t for all neighbours of the recently frozen cell and move them to the narrow band. If a neighbour is already in the narrow band, it is recomputed taking the recently frozen cell into account.
5. If the narrow band is not empty, go to step 3. The loop continues until all cells become frozen.

Difficulty of applying fast marching methods on unstructured grids

In unstructured finite element meshes, the connectivity between adjacent elements is not necessarily aligned with the coordinate axes. Elemental edges are addressed as edges for conciseness. We could use a linear combination of directional derivatives along edges to compute the gradient in Eq. 12 in an element. The propagation time and speed are defined on nodes and elements, respectively [56]. Let P denote the matrix storing in rows the vectors along edges and $\mathbf{t}_d$ denote the vector of directional derivatives of propagation time along edges in an element. We have

$$P\nabla t = \mathbf{t}_d . \tag{33}$$

Inserting Eq. 33 into Eq. 13 leads to

$$\mathbf{t}_d^T (P^{-1})^T F P^{-1} \mathbf{t}_d = 1 . \tag{34}$$

The dimension of $\mathbf{t}_d$ is two for 2D triangular meshes and three for 3D tetrahedral meshes. The directional derivatives are set to be piecewise constant on the edges. Consequently, Eq. 34 will always result in a quadratic equation for t regardless of the number of dimensions.

The problem with this method is the lack of monotonicity. Suppose we have a triangle ijm with the propagation time known at nodes i and j and unknown at node m. We could compute t_m using Eq. 34 and adopt the larger propagation time for t_m. However, t_m might be smaller than either t_i or t_j, which is against the principle of monotonicity. Therefore, [56] introduced a causality condition requiring that t_m can only be solved in adjacent triangles where both t_i and t_j are known and smaller than the computed t_m. However, the causality condition might not hold in any neighbouring triangles of a node in a mesh containing obtuse angles. As a result, FMM may terminate much earlier before sweeping the entire domain. Sethian and Vladimirsky [56] proposed a possible solution by splitting obtuse angles and building extra supportive triangles. However, the extension to 3D tetrahedral meshes is difficult.

An alternative finite element discretisation of the Eikonal equation on unstructured meshes is presented in [21].

Here, ∇t is discretised as $\nabla N_i t_i$ where N_i is a linear basis function. However, the same problem of fulfilling the causality condition arises. Thus, they modified the FMM algorithm and frozen a node as soon as it is computed as a candidate without building a narrow band, but this is against the principle of FMM and will produce inaccurate results in heterogeneous models.

Further, the causality condition may not be satisfied even on a Cartesian grid when the propagation speed is anisotropic with main axes not aligned with the connectivity between cells. Sethian and Vladimirsky [57] presented an enlarged neighbourhood method to include more cells for computing t when the causality condition fails. Konukoglu et al. [36] includes a recursive correction step in the FMM main loop where the neighbours of an updated node are recomputed such that the causality condition could be satisfied. However, it is not clear whether these methods can solve the monotonicity problem in unstructured tetrahedral meshes.

References

1. Abushaikha, A.S., Blunt, M.J., Gosselin, O.R., Pain, C.C., Jackson, M.D.: Interface control volume finite element method for modelling multi-phase fluid flow in highly heterogeneous and fractured reservoirs. J. Comput. Phys. **298**, 41–61 (2015)
2. Arnold, D., Demyanov, V., Christie, M., Bakay, A., Gopa, K.: Optimisation of decision making under uncertainty throughout field lifetime: A fractured reservoir example. Comput. Geosci. **95**, 123–139 (2016)
3. Baliga, B., Patankar, S.: A new finite-element formulation for convection-diffusion problems. Numer. Heat Transfer **3**(4), 393–409 (1980)
4. Bank, R., Falgout, R., Jones, T., Manteuffel, T.A., McCormick, S.F., Ruge, J.W.: Algebraic multigrid domain and range decomposition (amg-dd/amg-rd). SIAM J. Sci. Comput. **37**(5), S113–S136 (2015)
5. Batycky, R.P., Thiele, M.R., Baker, R.O., Chung, S.: Revisiting reservoir flood-surveillance methods using streamlines. SPE Paper 95402 (2005)
6. Bentley, M.: Modelling for comfort? Pet. Geosci. **22**(1), 3–10 (2016)
7. Bond, C., Gibbs, A., Shipton, Z., Jones, S.: What do you think this is? "Conceptual uncertainty" in geoscience interpretation. GSA Today **17**(11), 4 (2007)
8. Bourdet, D.: Well Test Analysis: the Use of Advanced Interpretation Models, vol. 3. Elsevier, Amsterdam (2002)
9. Caumon, G., Collon-Drouaillet, P., De Veslud, C.L.C., Viseur, S., Sausse, J.: Surface-based 3d modeling of geological structures. Math. Geosci. **41**(8), 927–945 (2009)
10. Cavero, J., Orellana, N.H., Yemez, I., Singh, V., Izaguirre, E.: Importance of conceptual geological models in 3d reservoir modelling. First Break **34**(7), 39–49 (2016)
11. Chandra, V.S., Corbett, P.W., Geiger, S., Hamdi, H., et al.: Improving reservoir characterization and simulation with near-wellbore modeling. SPE Reserv. Eval. Eng. **16**(02), 183–193 (2013)
12. Choudhuri, B., Thakuria, C., Belushi, A.A., Nurzaman, Z., Al Hashmi, K., Batycky, R.: Optimization of a large polymer flood with full-field streamline simulation. SPE Reserv. Eval. Eng. **18**(2), 318–328 (2015)
13. Corbett, P., Geiger, S., Borges, L., Garayev, M., Valdez, C.: The third porosity system understanding the role of hidden pore systems in well-test interpretation in carbonates. Pet. Geosci. **18**(1), 73–81 (2012)
14. Corbett, P.W., Geiger-Boschung, S., Borges, L.P., Garayev, M., Gonzalez, J.G., Valdez, C., et al.: Limitations in numerical well test modelling of fractured carbonate rocks. In: SPE EUROPEC/EAGE Annual Conference and Exhibition. Society of Petroleum Engineers (2010)
15. Corbett, P.W., Mesmari, A., Stewart, G., et al.: A method for using the naturally-occurring negative geoskin in the description of fluvial reservoirs. In: European Petroleum Conference. Society of Petroleum Engineers (1996)
16. Dahiya, D., Baskar, S., Coulouvrat, F.: Characteristic fast marching method for monotonically propagating fronts in a moving medium. SIAM J. Sci. Comput. **35**(4), A1880–A1902 (2013)
17. Datta-Gupta, A., King, M.J.: Streamline Simulation: Theory and practice. Vol. 11. Society of Petroleum Engineers Richardson (2007)
18. Datta-Gupta, A., Xie, J., Gupta, N., King, M.J., Lee, W.J., et al.: Radius of investigation and its generalization to unconventional reservoirs. J. Petrol. Tech. **63**(07), 52–55 (2011)
19. Edwards, M.G.: Higher-resolution hyperbolic-coupled-elliptic flux-continuous CVD schemes on structured and unstructured grids in 2-d. Int. J. Numer. Methods Fluids **51**(9-10), 1059–1077 (2006)
20. Egya, D., Geiger, S., Corbett, P., March, R., Bisdom, K., Bertotti, G., Bezerra, F.: Analysing the limitations of the dual-porosity response during well tests in naturally fractured reservoirs. Pet. Geosci. **25**, 30–49 (2019)
21. Elias, R.N., Martins, M.A., Coutinho, A.L.: Simple finite element-based computation of distance functions in unstructured grids. Int. J. Numer. Methods Eng. **72**(9), 1095–1110 (2007)
22. Forsyth, P.A., et al.: A control-volume, finite-element method for local mesh refinement in thermal reservoir simulation. SPE Reserv. Eng. **5**(04), 561–566 (1990)
23. Gomes, J., Pavlidis, D., Salinas, P., Xie, Z., Percival, J.R., Melnikova, Y., Pain, C.C., Jackson, M.D.: A force-balanced control volume finite element method for multiphase porous media flow modelling. International Journal for Numerical Methods Fluids, pp. 1097–0363 (2016)
24. Graham, G.H., Jackson, M.D., Hampson, G.J.: Three-dimensional modeling of clinoforms in shallow-marine reservoirs: part 1. Concepts and application clinoform modeling in shallow-marine reservoirs: Part 1. Concepts and application. AAPG Bull. **99**(6), 1013–1047 (2015)
25. Graham, G.H., Jackson, M.D., Hampson, G.J.: Three-dimensional modeling of clinoforms in shallow-marine reservoirs: part 2. Impact on fluid flow and hydrocarbon recovery in fluvial-dominated deltaic reservoirs. AAPG Bull. **99**(6), 1049–1080 (2015)
26. Gries, S.: On the convergence of System-AMG in reservoir simulation. SPE Paper 182630 (2017)
27. Hægland, H.: Streamline methods with application to flow and transport in fractured media. Ph.D. thesis, University of Bergen (2009)
28. Hægland, H., Kaufmann, R., Aavatsmark, I.: Comparison of vertex- and cell-centered methods for flow and transport simulation in 3d. SPE paper 163593 (2012)
29. Hassanpour, M.M., Pyrcz, M.J., Deutsch, C.V.: Improved geostatistical models of inclined heterolithic strata for McMurray

Formation, Alberta, Canada. AAPG Bull. **97**(7), 1209–1224 (2013)
30. Hoffman, K.S., Neave, J.W.: Horizon modeling using a three-dimensional fault restoration technique. SPE paper 56445 (1999)
31. Jackson, M., Hampson, G., Rood, D., Geiger, S., Zhang, Z., Sousa, M., Amorim, R., Brazil, E., Samavati, F., Guimaraes, L.: Rapid reservoir modeling: psrototyping of reservoir models, well trajectories and development options using an intuitive, sketch-based interface. SPE Paper 173237 (2015)
32. Jackson, M., Percival, J., Mostaghimi, P., Tollit, B., Pavlidis, D., Pain, C., Gomes, J., Elsheikh, A.H., Salinas, P., Muggeridge, A., Blunt, M.: Reservoir modeling for flow simulation by use of surfaces, adaptive unstructured meshes, and an overlapping-control-volume finite-element method. SPE Reserv. Eval. Eng. **18**(02), 115–132 (2015)
33. Jacquemyn, C., Jackson, M., Hampson, G.: Surface-based geological reservoir modelling using grid-free nurbs curves and surfaces. Mathematical Geosciences. https://doi.org/10.1007/s11004-018-9764-8 (2018)
34. Jacquemyn, C., Melnikova, Y., Jackson, M., Hampson, G., John, C.: Geologic modelling using parametric nurbs surfaces. In: ECMOR XV-15th European Conference on the Mathematics of Oil Recovery (2016)
35. Kimmel, R., Sethian, J.A.: Computing geodesic paths on manifolds. Proc. Natl. Acad. Sci. **95**(15), 8431–8435 (1998)
36. Konukoglu, E., Sermesant, M., Clatz, O., Peyrat, J.-M., Delingette, H., Ayache, N.: A recursive anisotropic fast marching approach to reaction diffusion equation: application to tumor growth modeling. In: Information Processing in Medical Imaging, pp. 687–699. Springer (2007)
37. Krogstad, S., Lie, K.-A., Nilsen, H.M., Berg, C.F., Kippe, V.: Efficient flow diagnostics proxies for polymer flooding. Comput. Geosci. **21**(5-6), 1203–1218 (2017)
38. Mallet, J.-L.: Geomodelling. Oxford University Press, Oxford (2002)
39. Massart, B.Y., Jackson, M.D., Hampson, G.J., Johnson, H.D., Legler, B., Jackson, C.A.-L.: Effective flow properties of heterolithic, cross-bedded tidal sandstones: part 1. Surface-based modeling. AAPG Bull. **100**(5), 697–721 (2016)
40. Massonnat, G., Bandiziol, D., et al.: Interdependence between geology and well test interpretation. In: SPE Annual Technical Conference and Exhibition. Society of Petroleum Engineers (1991)
41. Matringe, S.F., Juanes, R., Tchelepi, H.A.: Tracing streamlines on unstructured grids from finite volume discretizations. SPE J. **13**(4), 423–431 (2008)
42. Mello, U.T., Rodrigues, J.R.P., Rossa, A.L.: A control-volume finite-element method for three-dimensional multiphase basin modeling. Mar. Pet. Geol. **26**(4), 504–518 (2009)
43. Milliotte, C., Matthäi, S.: From seismic interpretation to reservoir model: an integrated study accounting for the structural complexity of the Vienna Basin using an unstructured reservoir grid. First Break **32**(5), 95–101 (2014)
44. Moog, G.: Advanced discretization methods for flow simulation using unstructured grids. Department of Energy Resources Engineering, Stanford University CA (2013)
45. Møyner, O., Krogstad, S., Lie, K.-A.: The application of flow diagnostics for reservoir management. SPE J. **20**(02), 306–323 (2015)
46. Natvig, J.R., Lie, K.-A., Eikemo, B., Berre, I.: An efficient discontinuous Galerkin method for advective transport in porous media. Adv. Water Resour. **30**(12), 2424–2438 (2007)
47. Olsen, L., Samavati, F.F., Sousa, M.C., Jorge, J.A.: Sketch-based modeling: a survey. Comput. Graph. **33**(1), 85–103 (2009)
48. Pyrcz, M.J., Boisvert, J.B., Deutsch, C.V.: Alluvsim: a program for event-based stochastic modeling of fluvial depositional systems. Comput. Geosci. **35**(8), 1671–1685 (2009)
49. Rankey, E.C., Mitchell, J.C.: That's why it's called interpretation: impact of horizon uncertainty on seismic attribute analysis. Lead. Edge **22**(9), 820–828 (2003)
50. Rasmussen, A.F.: Streamline tracing on irregular geometries. In: EC- MOR XII-12th European Conference on the Mathematics of Oil Recovery (2010)
51. Rood, M., Jackson, M., Hampson, G., Brazil, E., de Carvalho, F., Coda, C., Sousa, M., Zhang, Z., Geiger, S.: Sketch-based geologic modeling. In: AGU Fall Meeting Abstracts (2015)
52. Salinas, P., Pavlidis, D., Xie, Z., Pain, C.C., Jackson, M.: A double control volume finite element method with dynamic unstructured mesh optimization. SPE paper 182647 (2017)
53. Sech, R.P., Jackson, M.D., Hampson, G.J.: Three-dimensional modeling of a shoreface-shelf parasequence reservoir analog: part 1. Surface-based modeling to capture high-resolution facies architecture. AAPG Bulletin **93**(9), 1155–1181 (2009)
54. Sermesant, M., Konukoglu, E., Delingette, H., Coudière, Y., Chinchapatnam, P., Rhode, K., Razavi, R., Ayache, N.: An anisotropic multi-front fast marching method for real-time simulation of cardiac electrophysiology. Functional Imaging and Modeling of the Heart, 160–169 (2007)
55. Sethian, J.A.: A fast marching level set method for monotonically advancing fronts. Proc. Natl. Acad. Sci. **93**(4), 1591–1595 (1996)
56. Sethian, J.A., Vladimirsky, A.: Fast methods for the Eikonal and related Hamilton–Jacobi equations on unstructured meshes. Proc. Natl. Acad. Sci. **97**(11), 5699–5703 (2000)
57. Sethian, J.A., Vladimirsky, A.: Ordered upwind methods for static Hamilton–Jacobi equations: Theory and algorithms. SIAM J. Numer. Anal. **41**(1), 325–363 (2003)
58. Shahvali, M., Mallison, B., Wei, K., Gross, H.: An alternative to streamlines for flow diagnostics on structured and unstructured grids. SPE J. **17**(03), 768–778 (2012)
59. Sharifi, M., Kelkar, M., Bahar, A., Slettebo, T., et al.: Dynamic ranking of multiple realizations by use of the fast-marching method. SPE J. **19**(06), 1–069 (2014)
60. Shook, G.M., Mitchell, K.M.: A robust measure of heterogeneity for ranking earth models: The F PHI curve and dynamic Lorenz coefficient. SPE Paper 124625 (2009)
61. Si, H.: Tetgen, a Delaunay-based quality tetrahedral mesh generator. ACM Trans. Math. Softw. (TOMS) **41**(2), 11 (2015)
62. Spooner, V., Geiger, S., Dan, A.: Flow diagnostics for naturally fractured reservoirs. SPE Paper 190877 (2018)
63. Stüben, K., Clees, T., Klie, H., Lu, B., Wheeler, M.: Algebraic multigrid methods (AMG) for the efficient solution of fully implicit formulations in reservoir simulation. SPE Paper 105832 (2007)
64. Thiele, M.R., Batycky, R.: Water injection optimization using a streamline-based workflow. SPE Paper 84080 (2003)
65. Vasco, D., Keers, H., Karasaki, K.: Estimation of reservoir properties using transient pressure data: An asymptotic approach. Water Resour. Res. **36**(12), 3447–3465 (2000)
66. Velho, L., Zorin, D.: 4–8 subdivision. Comput. Aided Geom. Des. **18**(5), 397–427 (2001)
67. Xie, J., Yang, C., Gupta, N., King, M.J., Datta-Gupta, A., et al.: Depth of investigation and depletion in unconventional reservoirs with fast-marching methods. SPE J. **20**(04), 831–841 (2015)
68. Xie, J., Yang, C., Gupta, N., King, M.J., Datta-Gupta, A., et al.: Integration of shale-gas-production data and microseismic for fracture and reservoir properties with the fast marching method. SPE J. **20**(02), 347–359 (2015)

69. Yang, C., Vyas, A., Data-Gupta, A., Ley, B., Biswas, P.: Rapid multistage hydraulic fracture design and optimization in unconventional reservoirs using a novel fast marching method. J. Pet. Sci. Eng. **156**, 91–101 (2017)
70. Yang, J., Stern, F.: A highly scalable massively parallel fast marching method for the Eikonal equation. J. Comput. Phys. **332**, 333–362 (2017)
71. Zhang, X., Pyrcz, M.J., Deutsch, C.V.: Stochastic surface modeling of deepwater depositional systems for improved reservoir models. J. Pet. Sci. Eng. **68**(1-2), 118–134 (2009)
72. Zhang, Y., Bansal, N., Fujita, Y., Datta-Gupta, A., King, M.J., Sankaran, S., et al.: From streamlines to fast marching: rapid simulation and performance assessment of shale-gas reservoirs by use of diffusive time of flight as a spatial coordinate. SPE J. **21**(05), 1883–1898 (2016)
73. Zhang, Y., Yang, C., King, M.J., Datta-Gupta, A., et al.: Fast-marching methods for complex grids and anisotropic permeabilities: application to unconventional reservoirs. SPE Paper 163637 (2013)
74. Zhang, Z.: Unstructured mesh methods for stratified turbulent flows. Ph.D. thesis, Loughborough University (2015)
75. Zhang, Z., Geiger, S., Rood, M., Jacquemyn, C., Jackson, M., Hampson, G., De Carvalho, F.M., Silva, C.C.M.M., Silva, J.D.M., Sousa, M.C., et al.: A tracing algorithm for flow diagnostics on fully unstructured grids with multipoint flux approximation. SPE J. **22**(6), 1946–1962 (2017)